



# Selective methane production from visible-light-driven photocatalytic carbon dioxide reduction using the surface plasmon resonance effect of superfine silver nanoparticles anchored on lithium titanium dioxide nanocubes (Ag@Li<sub>x</sub>TiO<sub>2</sub>)

Jeong Yeon Do<sup>a</sup>, Rama Krishna Chava<sup>a</sup>, Kotesch Kumar Mandari<sup>a</sup>, No-Kuk Park<sup>b</sup>, Ho-Jung Ryu<sup>c</sup>, Myung Won Seo<sup>c</sup>, Doyeon Lee<sup>c</sup>, T.S. Senthil<sup>d</sup>, Misook Kang<sup>a,\*</sup>

<sup>a</sup> Department of Chemistry, College of Natural Sciences, Yeungnam University, Gyeongsan, Gyeongbuk 38541, Republic of Korea

<sup>b</sup> School of Chemical Engineering, Yeungnam University, Gyeongsan, Gyeongbuk 38541, Republic of Korea

<sup>c</sup> Korea Institute of Energy Research, 152 Gajeong-ro, Yuseong-gu, Daejeon, 34129, Republic of Korea

<sup>d</sup> Department of Physics, Erode Sengunthar Engineering College, Erode 638 057, India

## ARTICLE INFO

### Keywords:

Surface plasmon resonance

Ag@Li<sub>x</sub>TiO<sub>2</sub>

Cube

Carbon dioxide photoreduction

Methane

Charge separation

## ABSTRACT

This study focused on the results of applying the strong surface plasmon resonance (SPR) effect of silver (Ag) particles anchored on cubic phase Li<sub>x</sub>TiO<sub>2</sub> to the carbon dioxide (CO<sub>2</sub>) photoreduction reaction. The study demonstrated the importance of three aspects: First, the cubic TiO<sub>2</sub>, which activated the [101] facet, was successfully produced. Secondly, Li<sup>+</sup> ions were introduced as Frenkel defects in some lattices to create oxygen defects. These vacancies increased the adsorption of carbon dioxide and sped up the rate-determining step in the CO<sub>2</sub> reduction reaction. In other words, they induced the easy conversion of CO<sub>2</sub> to CO, which is the first reduction product. Finally, the loading of Ag nanoparticles onto the Li<sub>x</sub>TiO<sub>2</sub> cubic surface the improved photocatalytic activity through SPR effects, and in particular led to selective conversion of CO<sub>2</sub> to methane (CH<sub>4</sub>). Quantitatively, the yield of CH<sub>4</sub> from CO<sub>2</sub> using the Ag@Li<sub>0.075</sub>TiO<sub>2</sub> particles was 49 μmol/g after 10 h of reaction, which was 8.2 and 1.5 times higher than that of cubic TiO<sub>2</sub> (6 μmol/g) and Li<sub>0.075</sub>TiO<sub>2</sub> (33 μmol/g) under UV-light. Additionally, its activity did not decrease under visible lights of 420 and 620 nm with the similar CH<sub>4</sub> yields of 42 and 34 μmol/g after 10 h, respectively. In particular, the production ratio of CH<sub>4</sub> and CO using cubic TiO<sub>2</sub> and Li<sub>x</sub>TiO<sub>2</sub> were about 1:1, with no selectivity for either product. However, after metallic Ag nanoparticles were loaded, the product selectivity shifted towards CH<sub>4</sub>, and the product ratio of CH<sub>4</sub> to CO was about 3:1. Furthermore, the Ag@Li<sub>0.075</sub>TiO<sub>2</sub> particles exhibited a strong SPR effect (in particular, direct electron transfer), which contributed to maintaining the charge separation and the lifetime of the catalyst over a long period. Catalytic deactivation was not observed during five cycles of recycling tests.

## 1. Introduction

Even ten years ago, carbon dioxide was regarded as the culprit of global warming, and a great deal of money is spent worldwide on carbon capture and storage (CCS) technology to reduce or eliminate CO<sub>2</sub>. In recent years, however, most countries have begun to utilize carbon dioxide as a carbon energy source, and have focused on the use of carbon capture and utility (CCU) as the main method of CO<sub>2</sub> reduction. One attractive CCU technology is biomimetic artificial photosynthesis, which uses a photocatalyst and sunlight to decompose carbon dioxide and water to produce hydrocarbons, which could replace

existing fossil fuels [1]. However, great barriers remain to be overcome in the commercialization of this technology, namely, the efficiency and lifetime of the photocatalyst. In general, a photocatalyst should have both a semiconductor band structure for absorbing light and converting it into energy, and a catalytic surface for inducing a chemical reaction. The photocatalyst absorbs photons from sunlight, which excites the electrons of the valence band to the conduction band, thereby forming electron-hole pairs. In the valence band, oxygen is produced, and in the conduction band, hydrogen is produced. This hydrogen serves to reduce the carbon dioxide. For artificial photosynthesis, the minimum energy required for water decomposition is 1.23 eV (although practically,

\* Corresponding author.

E-mail address: [mskang@ynu.ac.kr](mailto:mskang@ynu.ac.kr) (M. Kang).

<https://doi.org/10.1016/j.apcatb.2018.06.070>

Received 18 February 2018; Received in revised form 24 June 2018; Accepted 26 June 2018

Available online 28 June 2018

0926-3373/ © 2018 Elsevier B.V. All rights reserved.

1.8 eV or more is required), and thus the size of the band gap is very important. Furthermore, there must be a redox potential between the valence band and the conduction band of the band-gap that corresponds to the hydrogen and oxygen evolution reaction [2]. When all these conditions are satisfied, the photocatalyst can be used for artificial photosynthesis.  $\text{TiO}_2$ ,  $\text{Fe}_2\text{O}_3$ ,  $\text{BiVO}_4$ ,  $\text{ZnO}$ , and  $\text{WO}_3$  are typical photocatalysts that meet these conditions [3–7].  $\text{TiO}_2$  is chemically stable and is the only commercially available catalyst for artificial photosynthesis, and is also used in sterilization, air purification, water treatment, and organic matter decomposition applications. However, in many studies, inefficient light absorption, rapid recombination of the charges generated by light, and the possibility of a reverse reaction have been reported, due to its wide band gap (2.8 to 3.2 eV). Therefore, catalysts such as  $\text{BiVO}_4$ ,  $\text{WO}_3$ , and  $\text{Fe}_2\text{O}_3$  have been attracting attention as chemically stable materials with smaller band-gaps of 2.2 to 2.6 eV. However, with the exception of  $\text{TiO}_2$ , no material with a lifetime of more than 10,000 h, which is required for commercialization, have been identified.

Recently,  $\text{TiO}_2$ -related research has focused on adjusting the band gap or improving the adsorption of reactants by controlling the morphology or defects in crystals [8,9]. For example, one method involves making a non-uniform junction on the surface by adjusting the crystal planes. In the case of anatase  $\text{TiO}_2$ , the order of the surface energies of the low index facets is  $[101] < [010] < [001]$ , which results in different catalytic activities for the facets. Researchers have reported that the photochemical carbon dioxide reductive activity increased on a 2D- $\text{TiO}_2$  nanosheet whose exposed facets were almost exclusively of the  $[101]$  type [10]. In particular, Li et al. reported [11] that loading Ag onto brookite  $\text{TiO}_2$  quasi-nanocubes with exposed  $[210]$  and  $[001]$  facets increased the activity and selectivity of the photoreduction of  $\text{CO}_2$  to  $\text{CO}/\text{CH}_4$ . They concluded that when the Ag-loading level is  $\leq 0.5\%$ , the small Ag nanoparticles are mainly dispersed on the  $[210]$  facets of the brookite nanocubes, resulting in an enhancement in the selectivity of CO generation; while  $> 0.5\%$  Ag-loading could lead to the formation of Ag nanoparticles aggregated on the  $[210]$  facets with some Ag nanoparticles dispersed on the  $[001]$  facets, causing greater selectivity for  $\text{CH}_4$  generation. Another strategy is to create defect sites on the  $\text{TiO}_2$  surface or to create a surface state that enhances the adhesion of  $\text{CO}_2$  to the surface to promote the reduction reaction. Typically, hydrogen plasma treatment is used to create oxygen vacancies [12], or to treat surfaces with non-noble metals, inorganic bases, or organic amines [13–15]. In recent years, the use of surface plasmon resonance (SPR) has been popular for improving the efficiency and lifetime of artificial photosynthetic catalysts. Plasmons are similar particles that vibrate in metal. They are attracting attention as a light absorption phenomenon in the visible region of metal particles or metamaterials, and they form a strong local electric field [16]. Plasmons have been studied in various fields such as optical waveguides, sensors, and light emitting devices, because they allow particles to collect light with a wavelength larger than the particle size. In particular, the use of plasmons is attracting attention due to the improved light absorptivity and photocurrent generation that can be achieved using this photoelectric phenomenon [17]. Recently, studies have been reported in which the efficiency of artificial photosynthesis was increased using the quantum phenomenon caused by SPR, which occurs when metal is exposed to light, allowing photocatalysts that are not normally sensitive to visible light to operate in visible light [18]. When SPR occurs, two important properties arise: the phenomenon of light trapping on the metal surface, and the phenomenon of excited electrons moving into the photocatalyst, resulting in large photocurrents. Initially, the enhancement of photocurrent by the SPR effect was reported mainly due to the light trapping effect of Au [19], Ag [20], and Cu [21] nanoparticles. Recently, however, SPR effects have also been reported in various metals and metal/metal oxide mixtures such as Al [22], Fe [23], Co [24], Ag/Ag<sub>2</sub>O [25], and Cu/Cu<sub>2</sub>O [26]. In particular, reports of the SPR of silver loaded  $\text{TiO}_2$  (Ag/ $\text{TiO}_2$ ) catalysts have been increasing rapidly, and these catalysts have shown

fairly good visible light activity in water splitting and organic decomposition [27,28]. However, the published reports did not completely reveal the evidence for SPR. In particular, an in-depth study of the effect of SPR on the photocatalytic reduction of  $\text{CO}_2$  is needed, as well as further investigation of the improvement in product selectivity, which one of the most important aspects of this catalytic reaction. Additionally, an in-depth investigation into the correlation between SPR and charge separation is required.

Thus, in this study, we tried to improve the  $\text{CO}_2$  photoreduction performance using all three of the methods described above: in order to activate the  $[101]$  facet having the smallest surface activation energy, tetra ethyl ammonium hydroxide was added as a capping agent to obtain nanocube-shaped  $\text{TiO}_2$ . In order to simultaneously introduce oxygen defects into the  $\text{TiO}_2$  lattice (so-called Frenkel defects), x moles of the organic base  $\text{Li}_2\text{O}$  were incorporated into the  $\text{TiO}_2$  crystal structure to form anatase  $\text{Li}_x\text{TiO}_2$  cubes. The addition of Li anions creates oxygen anion defect sites in the lattice, which can increase  $\text{CO}_2$  gas adsorption. In addition, we tried to induce the SPR effect by loading 1.0 wt.% of Ag nanoparticles onto  $\text{Li}_x\text{TiO}_2$ , expecting an improvement of the photocatalytic efficiency by the optical trap effect. In particular, we hoped to induce the selective production of  $\text{CH}_4$  by enhancing the hydrogen production capability of Ag ions that was reported in a previous study [29]. Four types of cubic  $\text{Li}_x\text{TiO}_2$  were synthesized in this study using a hydrothermal method by the addition of 2.5, 5.0, 7.5, and 10.0 mol.% of Li. The synthesis of Ag@ $\text{Li}_x\text{TiO}_2$  with an Ag loading of 1.0 wt.% Ag using the most optimal  $\text{Li}_x\text{TiO}_2$  particle was then carried out. The surface properties of the synthesized particles were characterized using various analytical techniques, and the particles were applied in the photoreduction of  $\text{CO}_2$ . Furthermore, the expected mechanisms for  $\text{CO}_2$  photoreduction by the SPR effect over the Ag@ $\text{Li}_x\text{TiO}_2$  particles under UV and visible radiation were described.

## 2. Experimental

### 2.1. Synthesis of anatase structured $\text{TiO}_2$ , $\text{Li}_x\text{TiO}_2$ , and Ag@ $\text{Li}_x\text{TiO}_2$ cubic particles

The  $\text{TiO}_2$ ,  $\text{Li}_x\text{TiO}_2$ , and Ag@ $\text{Li}_x\text{TiO}_2$  particles were prepared by a typical hydrothermal method. To prepare the sol-mixtures, titanium tetraisopropoxide (TTIP, 99.99%, Junsei Chemical, Japan), lithium hydroxide (LiOH, 99.99%, Junsei Chemical, Japan), and silver nitrate ( $\text{AgNO}_3$ , 99.99%, Junsei Chemical, Japan) were used as the Ti, Li, and Ag precursors, respectively. In the first step of the  $\text{TiO}_2$  synthesis, 1.0 mol of TTIP was dissolved in distilled water, and 2.0 mol of the capping agent tetra ethyl ammonium hydroxide were added slowly to the solution, and then stirred to homogeneity for 2 h. The final solution was transferred to an autoclave for thermal treatment at 200 °C at 10 atm for 1 h in a nitrogen environment. After thermal treatment, the resulting precipitate was collected, washed with acetic acid, and then dried at 80 °C for 24 h. In the second step, the synthesis of  $\text{Li}_x\text{TiO}_2$  particles was carried out similarly to the synthesis of  $\text{TiO}_2$ , but the molar percentage of Li ions in the starting materials was adjusted to 2.5, 5.0, 7.5, and 10.0 mol.%, corresponding to 1.0 mol of Ti ions. Consequently, four kinds of particles, which were named  $\text{Li}_{0.025}\text{TiO}_2$ ,  $\text{Li}_{0.05}\text{TiO}_2$ ,  $\text{Li}_{0.075}\text{TiO}_2$ , and  $\text{Li}_{0.1}\text{TiO}_2$ , were synthesized in this study. In final step, an amount of  $\text{AgNO}_3$  corresponding to 1.0 wt.% of the amount of  $\text{Li}_x\text{TiO}_2$  was dissolved in a beaker containing an ethanol solution in which the  $\text{Li}_x\text{TiO}_2$  catalyst was dispersed. After being dispersed well by stirring, a  $\text{NaBH}_4$  solution was slowly added over 2 h to reduce the Ag ions. The product was dried at 80 °C for 3 h and then further dried in a dry oven at 70 °C for 24 h. The obtained sample was named Ag@ $\text{Li}_x\text{TiO}_2$ .

### 2.2. Characterization of the $\text{TiO}_2$ , $\text{Li}_x\text{TiO}_2$ , and Ag@ $\text{Li}_x\text{TiO}_2$ cubic particles

The XRD diffraction patterns of the synthesized  $\text{TiO}_2$ ,  $\text{Li}_x\text{TiO}_2$ , and

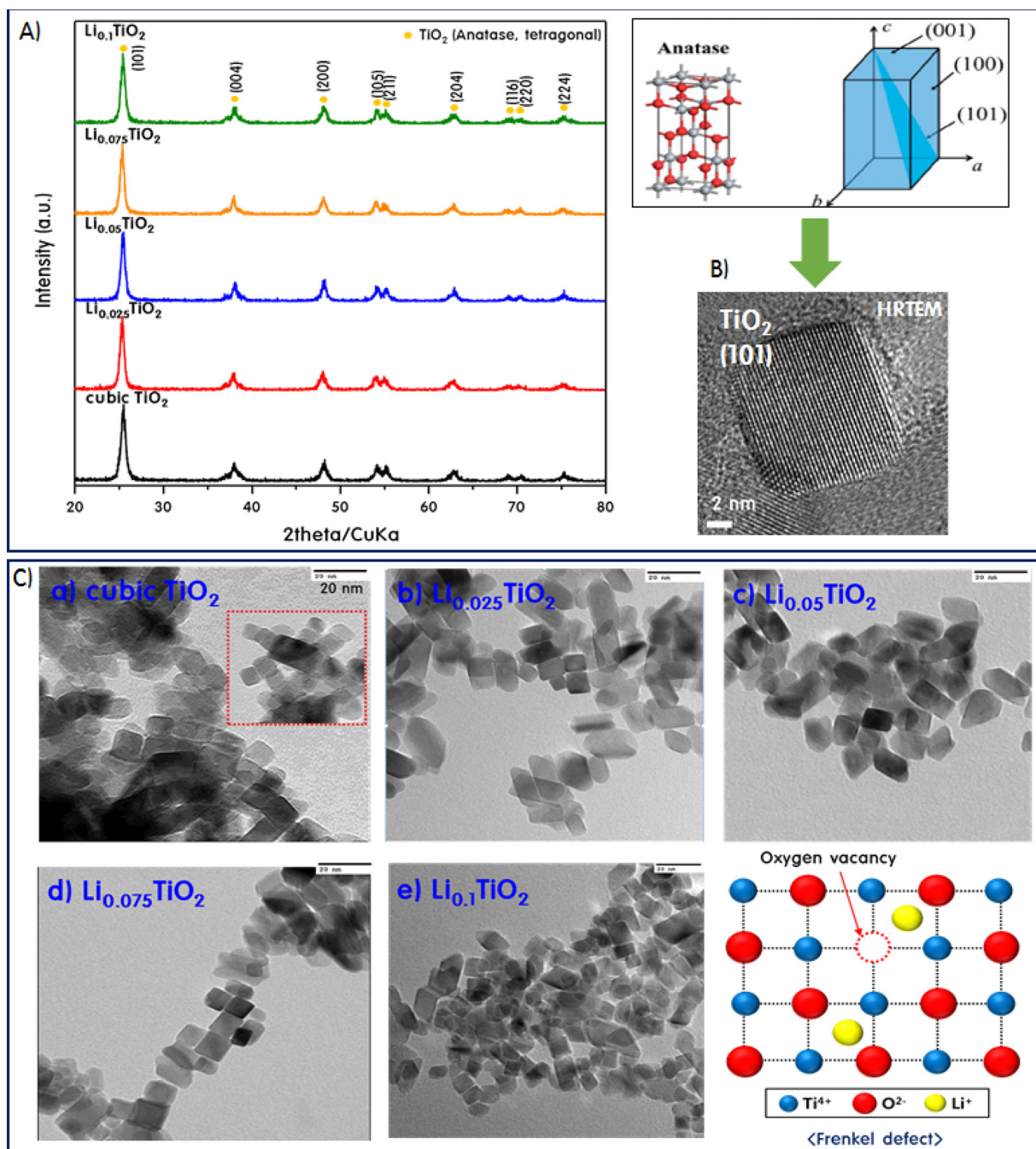


Fig. 1. XRD patterns (A), HRTEM (B), and TEM images (C) of  $\text{TiO}_2$  and  $\text{Li}_x\text{TiO}_2$  particles.

$\text{Ag@Li}_x\text{TiO}_2$  particles were recorded using an X'Pert Pro MPD PANalytical 2-circle diffractometer using nickel-filtered  $\text{CuK}\alpha$  ( $\lambda = 1.5406 \text{ \AA}$ ) radiation operating at 30 kV and 15 mA for a  $2\theta$  angle of diffraction range from  $10^\circ$  to  $80^\circ$  with an angular step of  $1^\circ\text{s}^{-1}$ . The morphology and atomic compositions of the  $\text{TiO}_2$  and  $\text{Li}_x\text{TiO}_2$  particles were observed using a transmission electron microscope (TEM, H-7600, Hitachi, Japan) and energy dispersive X-ray spectroscopy (EDS, EX-250, Horiba). The crystal lattice structure of the  $\text{Ag@Li}_x\text{TiO}_2$  particles was analyzed using a high-resolution transmission electron microscope (HRTEM, JEM-2100 F, Jeol) with the images being obtained at 200 kV. The X-ray photoelectron spectra (XPS) of the  $\text{Ag@Li}_x\text{TiO}_2$  particles were obtained using a Kratos Axis Nova instrument using monochromatic  $\text{AlK}\alpha$  radiation (225 W, 15 mA, 15 kV). The optical properties of the  $\text{TiO}_2$ ,  $\text{Li}_x\text{TiO}_2$ , and  $\text{Ag@Li}_x\text{TiO}_2$  particles were confirmed using diffuse-reflectance ultraviolet–visible spectrometer (UV–vis, Neosys-

2000, Scinco co. Korea) in the wavelength 200 to 800 nm range and photoluminescence spectroscopy (PL, Perkin Elmer, He–Cd laser source, wavelength of 300 nm). The number of electrons excited by light on the  $\text{TiO}_2$ ,  $\text{Li}_x\text{TiO}_2$ , and  $\text{Ag@Li}_x\text{TiO}_2$  particles was predicted from the photocurrent densities obtained using a sun 2000 solar simulator (IVIUM STAT, ABET technologies) under a red light-emitting diode (max. = 620 nm). Intensity-modulated photo voltage spectroscopy (IMVS) and intensity-modulated photocurrent spectroscopy (IMPS) were performed under open-circuit conditions to measure the electron and hole recombination properties and the electron transport time using a sun 2000 solar simulator (IVIUM STAT, ABET technologies) under illumination with power density of  $\text{AM1.5}$  ( $100 \text{ mW/cm}^2$ ). The outputs from the electronic cells that were fabricated using the synthesized particles were connected directly to a lock-in amplifier. The modulated intensity was  $> 1\%$  of the total light intensity. The



frequencies recorded were chosen logarithmically with 10 points per decade in the range 0.1–1000 Hz. Time constants were calculated using the frequency at which a minimum occurred in the imaginary response by using a non-linear fitting procedure. ESR (EPR) spectrometer (electron spin (paramagnetic) resonance, Bruker, EMXplus-9.5/2.7, Germany) was used to analyze the oxygen defects in particles at 9.3 GHz (X band) using a 100 kHz field modulation and a 0.5 G standard modulation width. The spectra were recorded at 77 K using a microwave power of 0.5 mW and accumulated 5 times. IPCE (incident photon to electron conversion efficiency (PEC-S20, Peccell Technologies, Inc., Japan) corresponds to the external quantum efficiency (QE) was measured to investigate the effect of excited electrons at each wavelength on photocatalytic efficiency.

### 2.3. Catalytic CO<sub>2</sub> photoreduction performance using TiO<sub>2</sub>, Li<sub>x</sub>TiO<sub>2</sub>, and Ag@Li<sub>x</sub>TiO<sub>2</sub> cubic particles

The CO<sub>2</sub> photoreduction activities of the synthesized TiO<sub>2</sub>, Li<sub>x</sub>TiO<sub>2</sub>, and Ag@Li<sub>x</sub>TiO<sub>2</sub> particles with H<sub>2</sub>O were carried out in a closed cylinder type quartz vessel (length, 15.0 cm; diameter, 1.0 cm; total volume, 12.50 mL). A schematic diagram of the photoreactor was provided in a previous publication [30]. Here, 0.2 g of the catalyst and 40.0 mL of distilled water were placed in the photoreactor. Supercritical fluid-grade CO<sub>2</sub> gas was used as the reactant, and the CO<sub>2</sub> gas was flowed into the chamber to purge air from the chamber before irradiation. The reactor chamber was then closed and the lamp was switched on. A UV-lamp (6 W/cm<sup>2</sup>, Shinan, Korea) with a 365-nm emitting light and a natural solar irradiation (a xenon lamp, 100 mW/cm<sup>2</sup>, 620 nm, 2000 solar simulator, ABET tech.) were used as the irradiation sources. Solar light intensity in solar simulator was calculated with the digital lux meter and the average light intensity was determined approximately i.e. 1,200,000 Lux. The photoreduction was carried out at room temperature and atmospheric pressure. The product gases were analyzed using a GC (gas chromatography, Master GC, Scinco, Korea) instrument equipped with thermal conductivity (TCD) and flame ionization detectors (FID) to separate the C<sub>1</sub>–C<sub>3</sub> light hydrocarbons and oxygenated compounds, such as CH<sub>4</sub>, CH<sub>3</sub>OH, HCHO, HCOOH, and CO. The product selectivity was calculated using the following equation: C<sub>i</sub> (%) = C<sub>i</sub> moles of the product/total moles of C produced × 100%. Furthermore, trace amounts of gases that are difficult to analyze by GC were analyzed using a Mass spectrometer (BELMASS, BEL Japan Inc., Japan).

## 3. Results and discussion

### 3.1. Physical properties of the cubic TiO<sub>2</sub> and Li<sub>x</sub>TiO<sub>2</sub> particles

Fig. 1 shows the X-ray diffraction patterns A), HRTEM B), and TEM images C) of pure TiO<sub>2</sub> and Li<sub>x</sub>TiO<sub>2</sub> particles doped with various molar ratios of Li that were synthesized in this study. In general, the TiO<sub>2</sub> anatase particles had spherical or rice-like shapes, which have been reported to have the body-centered tetragonal phase and longer z-axis of the I4<sub>1</sub> space group in many papers [31]. The TiO<sub>2</sub> (JCPDS code: 00-021-1272) synthesized in this study showed XRD peaks in the same positions as those of anatase; additionally, the obtained patterns also clearly demonstrated the absence of phase impurities, namely the rutile and brookite phases. The unique feature of the TiO<sub>2</sub> particles synthesized in this study was that the [101] (diagonal plane) peaks were very strong, but the growth of other crystal planes was relatively weak. This was because the capping agents added in the synthesis step inhibited the crystal growth along one axis, possibly the z-axis. This effect was expected to result in a shorter z-axis and a wider [101] facet. In other words, we expected to obtain cubic-shaped TiO<sub>2</sub>. As expected, cubic-shaped TiO<sub>2</sub> particles and the growth of [101] facet in the cubic TiO<sub>2</sub> are clearly observed in Fig. 1B and C. The mechanism by which the cubic shape of TiO<sub>2</sub> was produced in the synthesis process can be

explained as follows. TTIP was easily converted to Ti(OH)<sub>6</sub> by hydrolysis in DI water, and then two of the OH ligands of Ti(OH)<sub>6</sub> were substituted by R<sub>4</sub>NH<sub>4</sub><sup>+</sup>OH (tetraethyl ammonium hydroxide) to form Ti(OH)<sub>4</sub>(R<sub>4</sub>NH<sub>4</sub><sup>+</sup>O)<sub>2</sub>. Thereafter, a condensation reaction took place between water molecules, which produced the intermediate [TiO<sub>2</sub>]<sub>n</sub>-(R<sub>4</sub>NH<sub>4</sub><sup>+</sup>O)<sub>2</sub>. In the next step, the R<sub>4</sub>NH<sub>4</sub><sup>+</sup>O ions eventually decomposed during heating at 200 °C to generate TiO<sub>2</sub> seeds, which then grew into stable TiO<sub>2</sub> grains. Since the condensation reaction could not occur between two ligands of the terminal groups with the capping agent (R<sub>4</sub>NH<sub>4</sub><sup>+</sup>O)<sub>2</sub>, crystal growth was difficult along this axis. Therefore, crystal growth occurred only along the other two axes, resulting in a controlled cubic shape in the generated particle. As mentioned in the introduction, it is well known that reactants are easily adsorbed on the [101] facet of anatase TiO<sub>2</sub>, and that the surface activation energy for CO<sub>2</sub> is lower on this facet compared to other crystal facets [32]. If the [101] facet could be grown to a large extent in this study, the adsorption and catalytic reduction of CO<sub>2</sub> may be increased. Additionally, based on the fact that there was no shift of the peaks of the Li<sub>x</sub>TiO<sub>2</sub> crystals despite the addition of Li, the Li ions were believed to be contained in the spaces between the lattices, rather than being substituted into Ti sites. Therefore, the oxygen defects in the lattice of the Li<sub>x</sub>TiO<sub>2</sub> crystal were due to the charge balance effect of a non-stoichiometric charge defect (the Frenkel defects are illustrated in Fig. 1C). If the amount of lattice oxygen vacancies is excessive, an unstable structure may cause the collapse of the skeleton, but TiO<sub>2</sub> is known to have a certain degree of oxygen defects in its crystal structure, which have a favorable effect on photocatalytic activity [33]. On the other hand, as more Li was added, the size of the particles became smaller, as shown in Fig. 1C. This was because the crystals hardened due to oxygen defects. Additionally, the broadening of the XRD peaks also indicated a small crystal size; based on the main [101] peak, the crystallite sizes of the cubic TiO<sub>2</sub>, Li<sub>0.025</sub>TiO<sub>2</sub>, Li<sub>0.05</sub>TiO<sub>2</sub>, Li<sub>0.075</sub>TiO<sub>2</sub>, and Li<sub>0.1</sub>TiO<sub>2</sub> particles calculated using Scherrer's equation [34] were 13.6, 14.2, 14.3, 14.5, and 13.6 nm, respectively. Ultimately, the XRD and TEM results were complementary and in good agreement.

Fig. 2 displays the UV–vis spectra A) and Tauc plots B) of the cubic TiO<sub>2</sub> and Li<sub>x</sub>TiO<sub>2</sub> particles, which were used to determine their band-gaps. The band-gap can be affected by the particle size, crystal defects, and the interference of scattered light [35]. The absorption bands corresponding to the octahedral symmetry of Ti<sup>4+</sup> in cubic TiO<sub>2</sub> (Fig. 2A) appeared at approximately 275 nm and 350 nm, as observed in previous reports [36], and were assigned to ligand (p-orbital) to metal (d-orbital) charge transfer and to d(T<sub>2g</sub>)–d(E<sub>g</sub>) transfer in the d-orbital of titanium. The absorption bands of the cubic Li<sub>x</sub>TiO<sub>2</sub> particles seemed to shift slightly to shorter wavelengths compared to that of pure cubic TiO<sub>2</sub>. However, the absorption of the tail part seemed to move toward longer wavelength as higher concentrations of the Li ion were added. The band-gaps in semiconductor materials are closely related to the wavelength range that they absorb, with the band-gap decreasing with increasing absorption wavelength. The absorbance curves were converted to Tauc plots and are shown in Fig. 2B, and the band-gaps, which were measured by extrapolating the absorbance region to determine the photon energy, were calculated to be approximately 3.09, 3.11, 3.10, 3.13, and 3.12 eV for the cubic TiO<sub>2</sub>, Li<sub>0.025</sub>TiO<sub>2</sub>, Li<sub>0.05</sub>TiO<sub>2</sub>, Li<sub>0.075</sub>TiO<sub>2</sub>, and Li<sub>0.1</sub>TiO<sub>2</sub> particles, respectively. In conclusion, since the Li ions were not substituted into the Ti atomic positions of the crystal structure, the absorbance was not particularly dependent on the amount of Li added.

Fig. 3 shows the PL spectra A) and photocurrent curves B) of the cubic TiO<sub>2</sub> and Li<sub>x</sub>TiO<sub>2</sub> particles. In a semiconductor material, electrons from the valence band are transferred to the conduction band, after which the excited electrons are stabilized by photoemission. If the number of emitted electrons resulting from recombination between excited electrons and holes increases, eventually, the photoactivity will decrease [37]. Additionally, the PL intensity can decrease greatly when a metal in a semiconductor can capture the excited electrons or has a

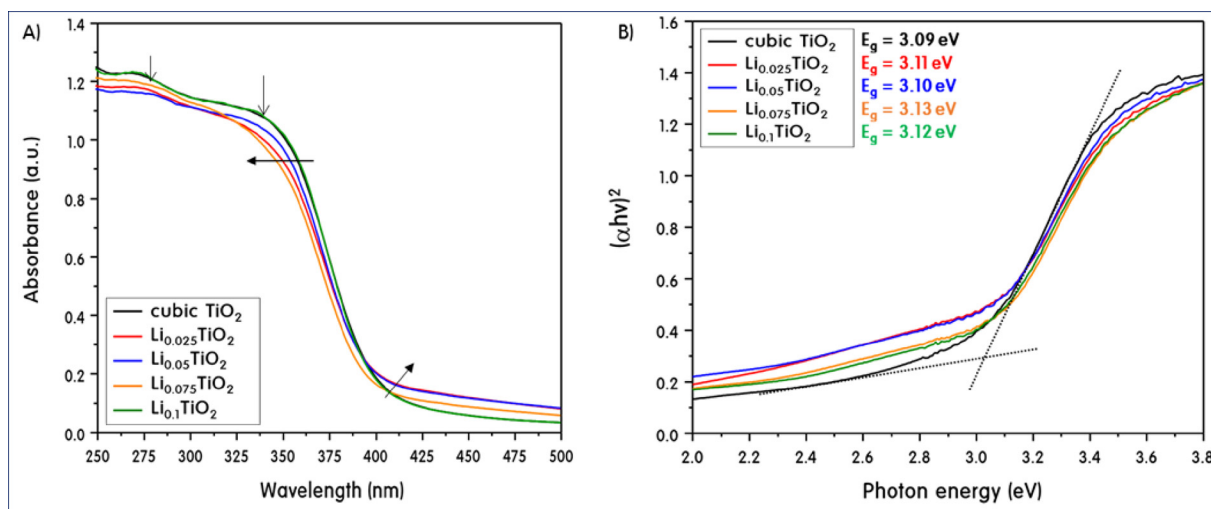


Fig. 2. UV-vis spectra (A) and Tauc plots (B) of TiO<sub>2</sub> and Li<sub>x</sub>TiO<sub>2</sub> particles.

high conductivity. In this study, it was found that when the particles were excited using a 340 nm LED light source, relaxation of each particle occurred at the three wavelengths of 400, 450 and 470 nm, as shown in Fig. 3A. Under these conditions, the pure cubic TiO<sub>2</sub> exhibited the strongest intensity, which means that the recombination between electrons and holes was the greatest. The PL intensity then decreased in the order Li<sub>0.1</sub>TiO<sub>2</sub> > Li<sub>0.025</sub>TiO<sub>2</sub> > Li<sub>0.05</sub>TiO<sub>2</sub> > Li<sub>0.075</sub>TiO<sub>2</sub>. In conclusion, the fact that the electron-hole recombination was the smallest for Li<sub>0.075</sub>TiO<sub>2</sub> means that these particles are expected to retain their catalytic activity for the longest time. In addition to PL, photocurrent measurement is another analytical method for studying charge separation. Typical real-time photocurrent responses of cubic TiO<sub>2</sub> and Li<sub>x</sub>TiO<sub>2</sub> particles to a light source being switched on and off are depicted in Fig. 3B. In general, a response is generated when photo-generated electron-hole pairs are separated, and illumination produces an increase in the current, which might result from photocarrier generation as well as carrier mobility enhancement [38]. When the light was turned on, the photoreduction current rapidly increased, and then reached a steady state after a few seconds. When the light was turned off, the photocurrent decreased instantaneously to almost zero. Under illumination, the pure cubic TiO<sub>2</sub> exhibited the lowest photocurrent up to the 4<sup>th</sup> cycle, which is typical of intrinsic semiconductors, and the

response steady rapidly over time, indicating stabilization of the catalyst. On the other hand, the current densities of Li<sub>x</sub>TiO<sub>2</sub> were very high throughout all cycles compared to pure TiO<sub>2</sub>. In particular, the signal for Li<sub>0.075</sub>TiO<sub>2</sub> (16.5 mA/cm<sup>2</sup>) was the highest after the 4<sup>th</sup> on-off cycle, and its value was 12 times higher than that of pure TiO<sub>2</sub> (1.3 mA/cm<sup>2</sup>), suggesting that the recombination of electrons and holes was suppressed in these particles.

Fig. 4 shows the CO<sub>2</sub> gas adsorption capacity of cubic TiO<sub>2</sub> and Li<sub>x</sub>TiO<sub>2</sub> particles. The particles were treated at 300 °C for 30 min to remove impurities, and CO<sub>2</sub> gas was adsorbed at 50 °C for 2 h. The temperature was increased to 450 °C at a rate of 5 °C/min to determine the desorption temperature, and the desorption curve and the adsorption amount of CO<sub>2</sub> gas per gram of the sample were calculated from the desorption area. The results indicated that the CO<sub>2</sub> gas was desorbed at approximately 350 °C, and that the desorption temperature increased slightly with the concentration of Li added. The amount of CO<sub>2</sub> gas adsorbed on all the Li<sub>x</sub>TiO<sub>2</sub> particles was greater than that of pure TiO<sub>2</sub>; the amount of CO<sub>2</sub> gas adsorbed on pure TiO<sub>2</sub> was 34.11 mmol/g, whereas the adsorption amounts of the catalysts Li<sub>0.025</sub>TiO<sub>2</sub>, Li<sub>0.05</sub>TiO<sub>2</sub>, Li<sub>0.075</sub>TiO<sub>2</sub>, and Li<sub>0.1</sub>TiO<sub>2</sub> were 36.57, 37.37, 41.10, and 38.42 mmol/g, respectively. Except for Li<sub>0.1</sub>TiO<sub>2</sub>, the amount of CO<sub>2</sub> gas adsorbed increased with increasing Li content. As

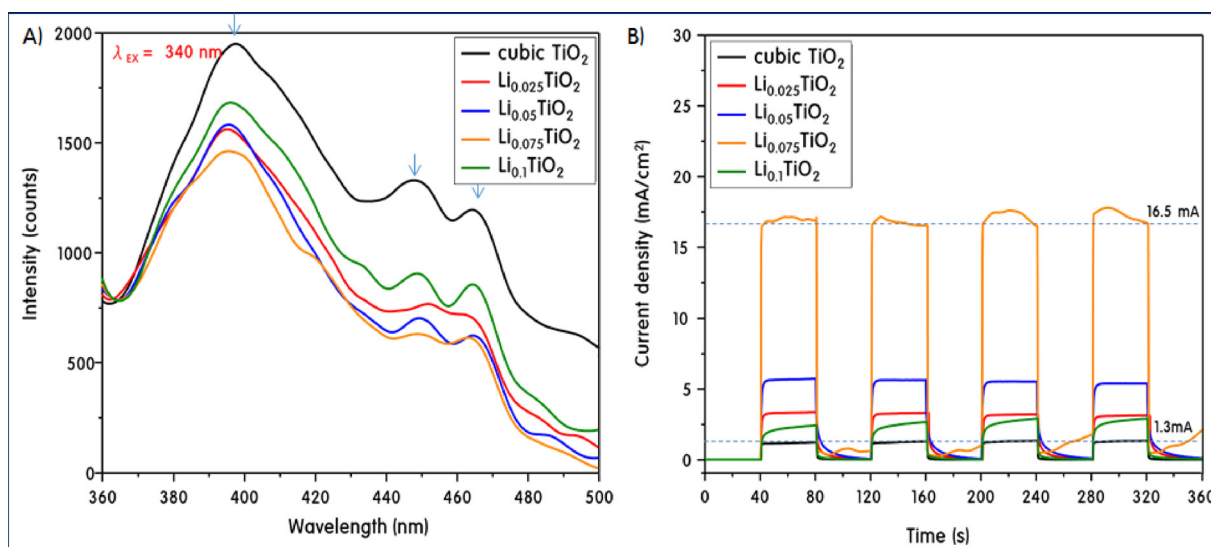


Fig. 3. PL spectra (A) and photocurrent curves (B) of TiO<sub>2</sub> and Li<sub>x</sub>TiO<sub>2</sub> particles.

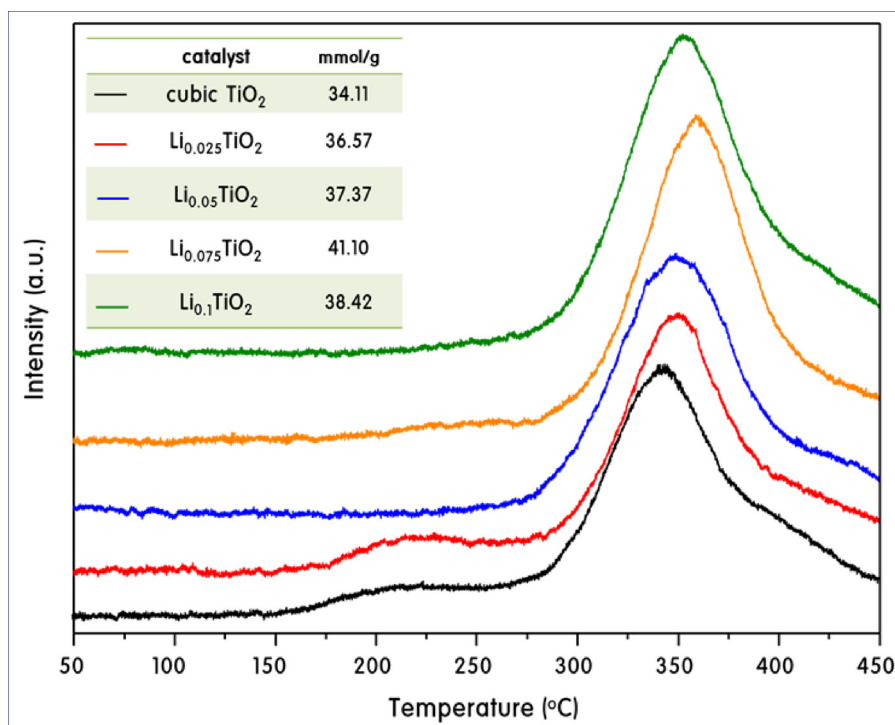


Fig. 4. CO<sub>2</sub> gas adsorption capacities of TiO<sub>2</sub> and Li<sub>x</sub>TiO<sub>2</sub> particles.

noted above, the addition of Li within the lattice increases the amount of oxygen vacancies in the lattice due to charge balancing. CO<sub>2</sub> is expected to be adsorbed in the vacant oxygen sites, and therefore, the greater the amount of oxygen vacancies, the stronger the attraction of CO<sub>2</sub> gases to the particle. However, as observed in the XRD results, excessive addition of Li (in the case of Li<sub>0.1</sub>TiO<sub>2</sub>) can lead to excessive oxygen deficiency, causing crystal face collapse, which may reduce the number of surface adsorption sites for CO<sub>2</sub>.

### 3.2. Catalytic performance of the cubic TiO<sub>2</sub> and Li<sub>x</sub>TiO<sub>2</sub> particles

The CO<sub>2</sub> photoreduction reaction was carried out under 365 nm light using cubic TiO<sub>2</sub> and Li<sub>x</sub>TiO<sub>2</sub> particles. Products that were difficult to detect by GC were measured by mass spectroscopy, and the results are shown in Fig. 5A and B. The main products generated by the photocatalytic reduction from CO<sub>2</sub> were confirmed to be CH<sub>4</sub> and CO by GC, and the product ratio of CH<sub>4</sub> and CO was unquestionably unselective (about 1:1) for all particles. In addition, the TiO<sub>2</sub>, Li<sub>0.025</sub>TiO<sub>2</sub>, and Li<sub>0.1</sub>TiO<sub>2</sub> particles produced fewer products per volume of injected CO<sub>2</sub>, suggesting that a large amount of CO<sub>2</sub> remained unreacted; the sum of the reduction products CH<sub>4</sub> and CO was less than 20 μmol/g after 10 h. However, using the Li<sub>0.05</sub>TiO<sub>2</sub> particles containing 5 mol.% of Li, 45 μmol/g of product was obtained after 10 h of reaction, and 65.0 μmol/g of product was obtained using Li<sub>0.075</sub>TiO<sub>2</sub> particles containing 7.5 mol.% Li after 10 h of reaction. On the other hand, as shown in Fig. 5B, additional products not detected by GC, such as CH<sub>3</sub>OH, HCOOH, H<sub>2</sub>, and O<sub>2</sub>, were clearly observed in the Mass spectra, and the intermediate CH<sub>2</sub> was identified. Greater amounts of these products were measured for the Li<sub>0.075</sub>TiO<sub>2</sub> particles than for the TiO<sub>2</sub> particles.

### 3.3. Effect of Ag addition to Li<sub>0.075</sub>TiO<sub>2</sub> particle (Ag@Li<sub>0.075</sub>TiO<sub>2</sub>)

In this work, we sought to determine a way to selectively obtain a single product rather than various reduction products. One potential method to achieve this is to promote the production of H<sub>2</sub> by water decomposition, which should increase the production of CH<sub>4</sub> compared to CO. Therefore, Ag was selected as a hydrogen generation promoter,

and the coating the metallic Ag<sup>o</sup> onto the Li<sub>0.075</sub>TiO<sub>2</sub> particles was carried out. Furthermore, we hoped to obtain a dual benefit through the SPR effect of Ag. Additionally, we expected the oxygen deficient sites would provide stable locations for the Ag particles to grow on the Li<sub>0.075</sub>TiO<sub>2</sub> surface (only used as much as the added amount), partially. In the next step, we investigated the effect of coating Ag onto Li<sub>0.075</sub>TiO<sub>2</sub> particles, which showed the best CO<sub>2</sub> reduction performance in Fig. 5. The synthesis method is presented in the experimental section.

Fig. 6 compares the XRD patterns A), UV–vis spectra B), and photocurrents C) of the Li<sub>0.075</sub>TiO<sub>2</sub> and Ag@Li<sub>0.075</sub>TiO<sub>2</sub> particles. Ag@Li<sub>0.075</sub>TiO<sub>2</sub> exhibited a perfect tetragonal anatase crystal structure like that of Li<sub>0.075</sub>TiO<sub>2</sub>, and the successful formation of Ag nanoparticles was also confirmed by the diffraction peaks at  $2\theta = 38.1^\circ$  and  $77.4^\circ$  corresponding to the [111] and [311] facets with a face centered cubic (FCC) structure attributed to metallic Ag<sup>o</sup> (JCPDS no 03-065-8428) [39]. The fact that peaks corresponding to metallic Ag were seen despite the very small Ag content of 1.0 wt.% indicates that Ag was grown on the Li<sub>0.075</sub>TiO<sub>2</sub> surface in a stable manner, that is, above the oxygen defects of the Li<sub>0.075</sub>TiO<sub>2</sub>. The diffraction peaks confirmed the stability of the synthesized Ag crystals, which is an important characteristic that promotes visible light photoexcitation. The most important feature of Ag nanoparticles with an SPR effect is the diffuse reflectance absorption spectra at 450 nm or above, which has been submitted as evidence of SPR in many reports [40]. In this study, the absorption band of the Ag@Li<sub>0.075</sub>TiO<sub>2</sub> particles also appears to be broad at 460 nm or higher, as shown in Fig. 6B. Finally, another feature associated with Ag SPR is the increase in photocurrent [41]. In Fig. 6C, the photocurrent (under visible light) of the Li<sub>0.075</sub>TiO<sub>2</sub> particles was 16.5 mA/cm<sup>2</sup> after 4 cycles, while that of the Ag@Li<sub>0.075</sub>TiO<sub>2</sub> was 57 mA/cm<sup>2</sup>, representing a 3.5-fold increase. The surprising increase in the photocurrent with the addition of 1.0 wt.% Ag coating could potentially be attributed to the perfect connection between Ag and Li<sub>0.075</sub>TiO<sub>2</sub>. That is, the loading of the Ag particles on the surface of Li<sub>0.075</sub>TiO<sub>2</sub> was stable, and the plasmons generated by the stable Ag particles at the defect sites on the surface were transferred to the conduction band of Li<sub>0.075</sub>TiO<sub>2</sub> without loss.

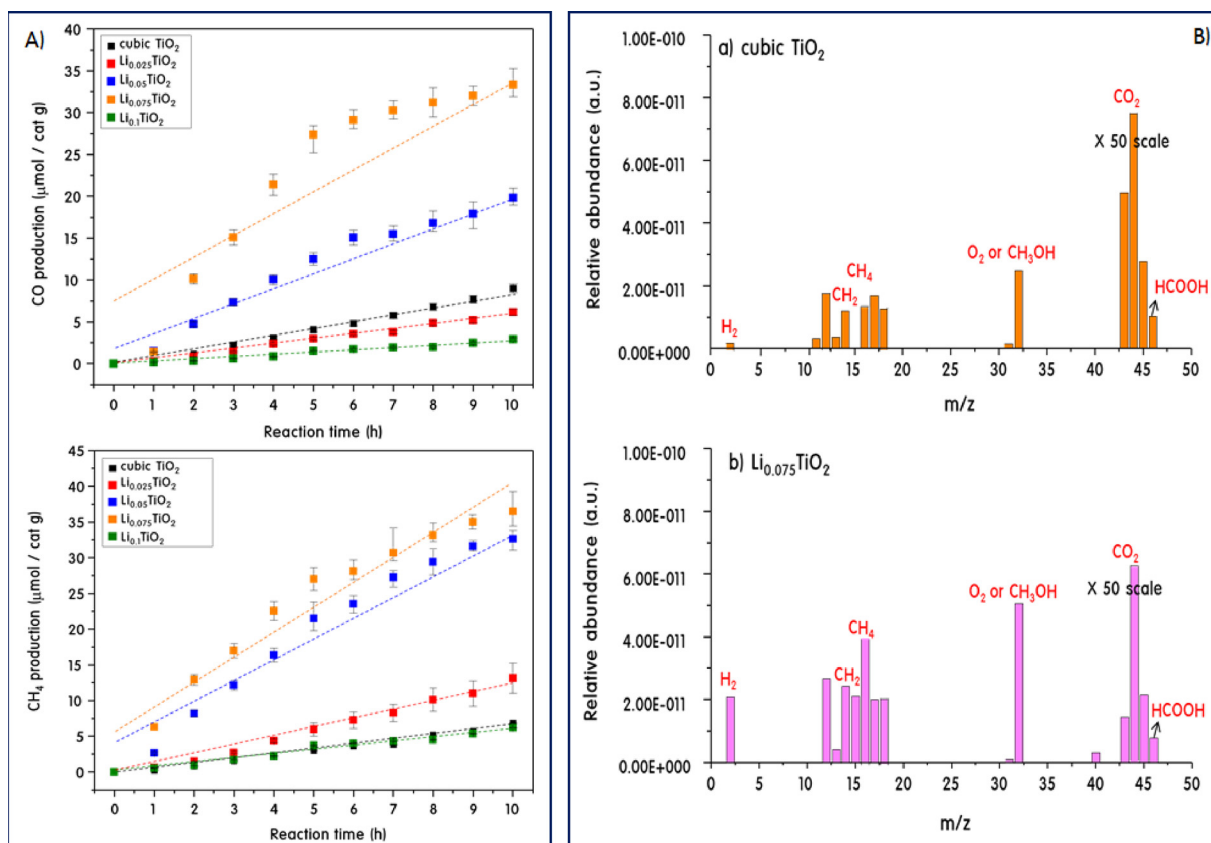


Fig. 5. Catalytic performances for CO<sub>2</sub> photoreduction under UV-light on TiO<sub>2</sub> and Li<sub>x</sub>TiO<sub>2</sub> particles (A) and product distributions measured by mass spectroscopy (B).

The Ag@Li<sub>0.075</sub>TiO<sub>2</sub> nanostructure was characterized using HRTEM, as shown in Fig. 7. The fringe spacing parallel to the nanocube was estimated to be 3.56 Å, which indicates that the crystal growth occurred preferentially in the [101] direction. The selected area electron diffraction (SAED) pattern of cubic TiO<sub>2</sub> recorded on the regularly spaced nanocubes exhibited diffraction rings, thereby indicating that the nanocubes are polycrystalline and can be readily indexed as the TiO<sub>2</sub> phase. The relatively uniform cubic particle exhibited a size of 10–20 nm. The Ag cubic structures were observed as very small black spots, and superfine Ag particles approximately 0.3 to 0.5 nm in size were found to exist stably on the [101] facet of Li<sub>0.075</sub>TiO<sub>2</sub>. However, the 1.0 wt.% loading of Ag was too low to determine clearly whether the growths of [111] or [311] cubic facets are occurred. Moreover, the Ag particles seemed to have settled in cages, rather than lying on the [101] plane. We predicted that the Ag particle was stably grown on the oxygen defects in the Li<sub>0.075</sub>TiO<sub>2</sub> lattice. Many research groups have reported that Ag particles have exhibited the strongest SPR effect when they have a size of 10 to 100 nm, and furthermore, it has been found that the absorption wavelength affecting SPRs also varies depending on the crystal morphologies of Ag [42,43]. This means that when the Ag particle sizes are changed, the growth facets are changed, and as a result, the activation energies of the reactants reacting with the exposed facets also change, so that the kinds of products produced are also changed. However, in this study, it is not easy to discuss the Ag particle size and SPR intensity because Ag particles are not larger than 10 nm because Ag is used as little as possible and dispersed to the maximum extent. As a result, the Ag-size dependence of SPRs is limited in the small particles due to physicochemical complexity and sample uncertainty. Peng et al. have analyzed the optical properties of very small Ag nanoparticles of 2 to 20 nm in a very uniform [44]: the behavior of the synthesized Ag particles was in good agreement with the multilayer Mie theory model. The SPR absorption band of highly dispersed small

size Ag particles was blue-shifted in size from 20 nm to 12 nm, but Ag particles smaller than 12 nm was strongly red-shifted (320 to 600 nm). On the other hand, the Ag particles synthesized in our study were very small, about 0.5 nm, and exhibited absorption bands above 460 nm. Therefore, it was somewhat unreasonable in our study to explain the relationship between the size of Ag nanoparticles and the intensity of SPR. However, it is clear that there was SPR effect even though it was a very small Ag particle. Meanwhile, TEM element mapping of Ag, Ti, and O atoms confirmed that these elements were well dispersed over the particle surface, and was well suited to stoichiometry. However, unfortunately, microscopy did not provide information related to Li.

Typical high-resolution quantitative XPS spectra of cubic TiO<sub>2</sub>, Li<sub>0.075</sub>TiO<sub>2</sub>, and Ag@Li<sub>0.075</sub>TiO<sub>2</sub> particles are presented in Fig. 8. The Ti2p<sub>1/2</sub> and Ti2p<sub>3/2</sub> spin orbital splitting photoelectrons were located at binding energies of 463.86 and 458.15 eV in cubic TiO<sub>2</sub>. For cubic TiO<sub>2</sub>, the curves were slightly shifted to a lower binding energy compared to common anatase structured TiO<sub>2</sub> [45], indicating that the Ti oxidation state was slightly altered by the crystal morphology and, hence, that the Ti–O bonding was weaker in cubic TiO<sub>2</sub> according to the hard-soft acid base (HSAB) rules, thereby resulting in easier electron flow. In Li<sub>0.075</sub>TiO<sub>2</sub>, the Ti2p<sub>3/2</sub> and Ti2p<sub>1/2</sub> binding energies were shifted to 457.12 and 462.82 eV. In general, a lower binding energy indicates a less oxidized state [46]. This indicates that oxygen atoms were released from the crystal lattice due to the addition of Li<sup>+</sup> ions, causing the reduction of Ti<sup>4+</sup> to Ti<sup>3+</sup>. However, in Ag@Li<sub>0.075</sub>TiO<sub>2</sub>, the binding energies shifted back to 457.60 and 463.36 eV for Ti2p<sub>3/2</sub> and Ti2p<sub>1/2</sub>. As discussed in the HRTEM section above, this was probably due to the addition of 1.0 wt.% of Ag and the resulting growth of Ag nanoparticles on the oxygen vacancy sites, which could attract electrons from the Ti ions to re-oxidize the Ti<sup>3+</sup>. Generally, the O1s region consisted of two main contributions, Ti–O (529.35 eV) and Ti–OH (hydroxyl group or oxygen vacancy, 531.5 eV) in pure cubic TiO<sub>2</sub> [47]. In Li<sub>0.075</sub>TiO<sub>2</sub>, the



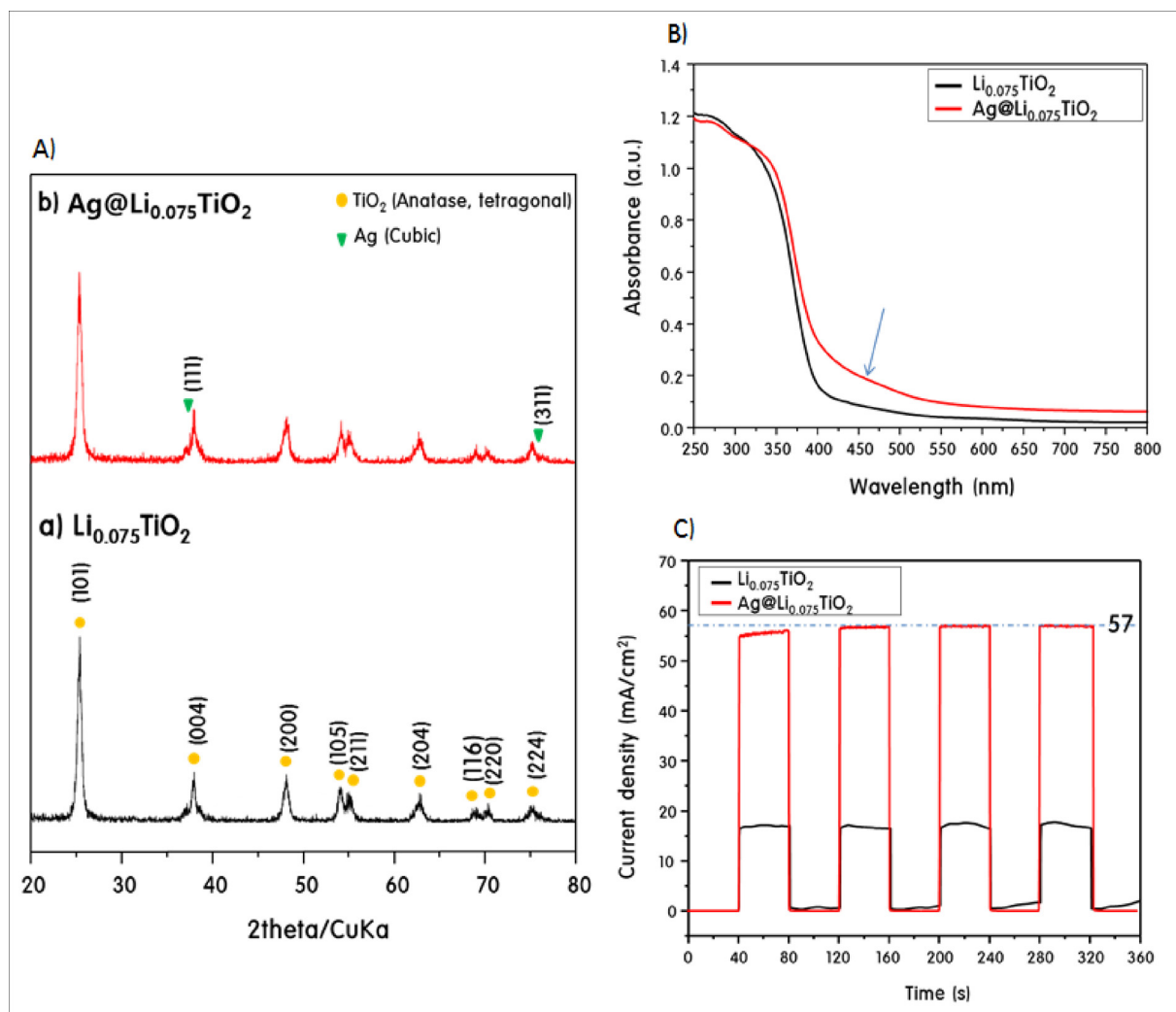


Fig. 6. XRD patterns (A), UV-vis spectra (B), and photocurrent (C) of  $\text{Li}_{0.075}\text{TiO}_2$  and  $\text{Ag}@\text{Li}_{0.075}\text{TiO}_2$  particles.

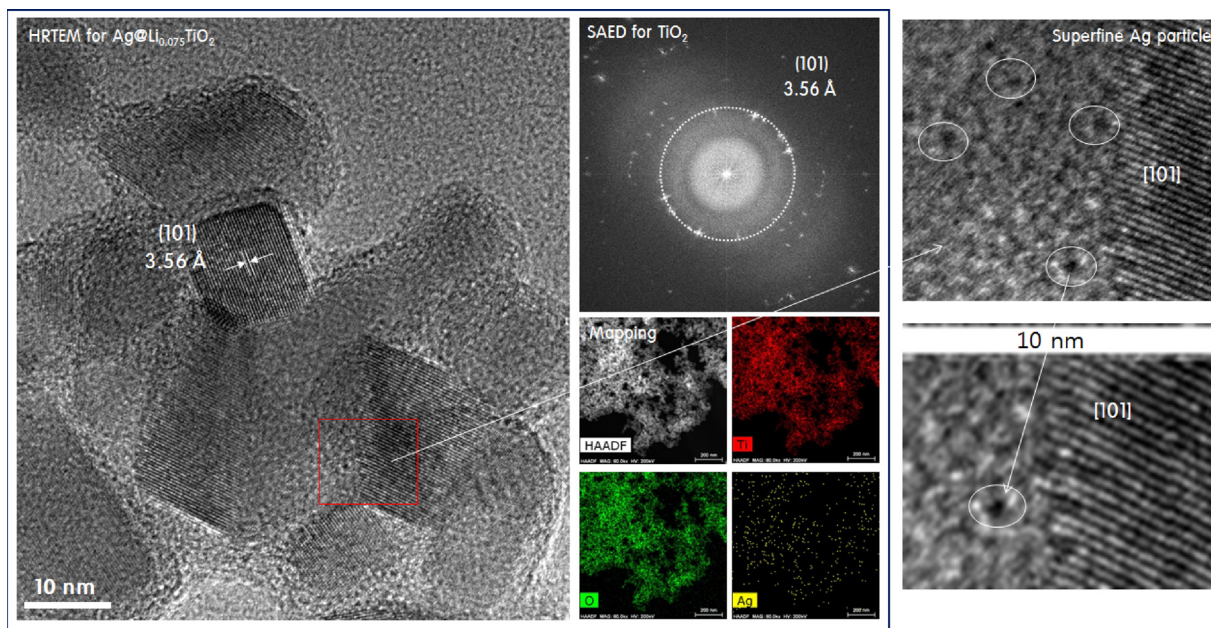


Fig. 7. HRTEM image of  $\text{Ag}@\text{Li}_{0.075}\text{TiO}_2$  particle.



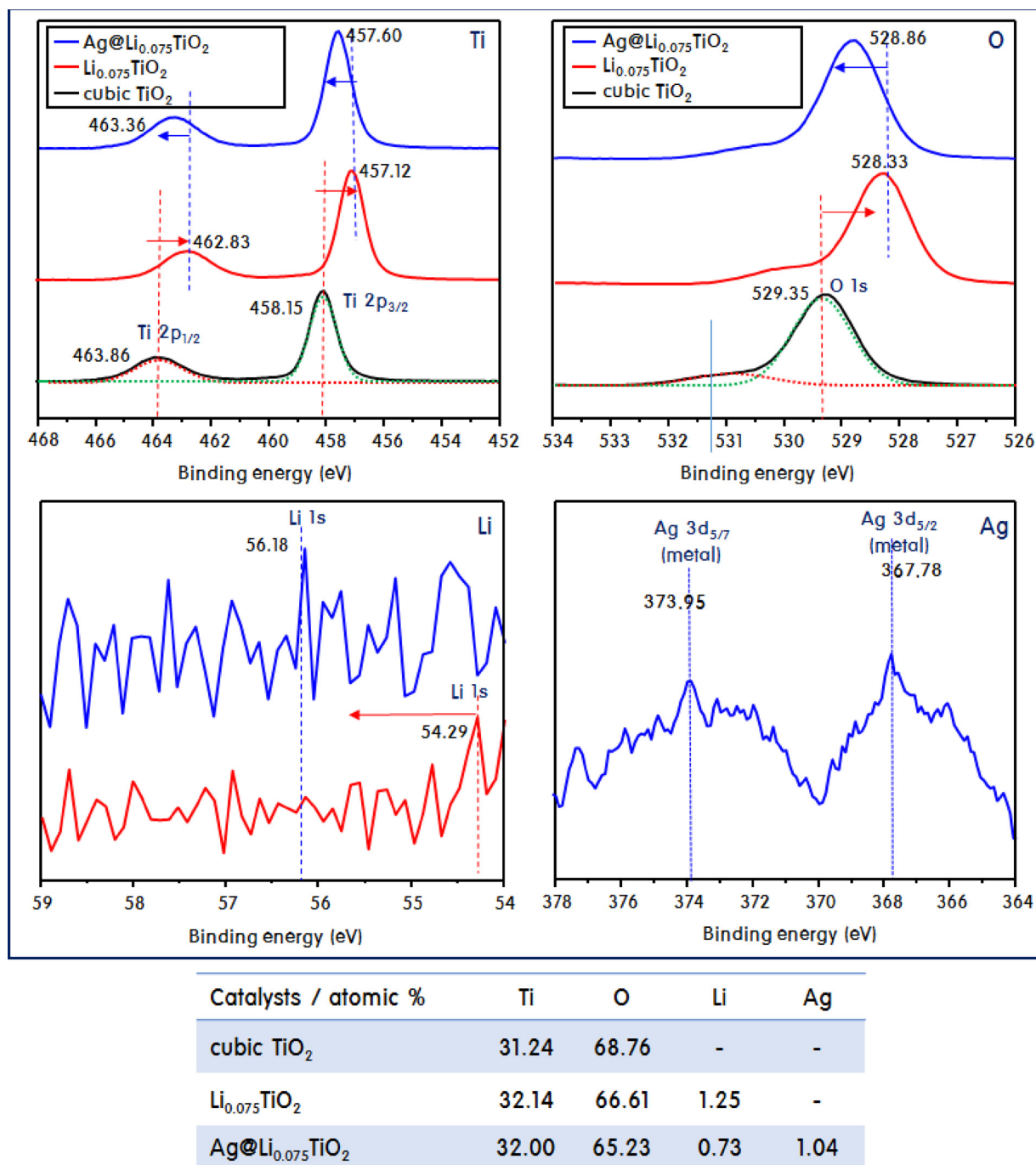


Fig. 8. XPS spectra for Ti2p, O1 s, Ag3d, and Li1 s in TiO<sub>2</sub>, Li<sub>0.075</sub>TiO<sub>2</sub>, and Ag@Li<sub>0.075</sub>TiO<sub>2</sub> particles.

O1 s peak migrated to a lower binding energy, 528.33, and it returned to a slightly higher energy of 528.86 eV in Ag@Li<sub>0.075</sub>TiO<sub>2</sub>. As mentioned in the discussion of the Ti2p binding energies above, in Li<sub>0.075</sub>TiO<sub>2</sub>, the addition of Li ions created oxygen defects in the lattice as Frenkel defects, which resulted in a decrease in the binding energy of O1 s. However, the added 1.0 wt.% of Ag resulted in the growth of Ag nanoparticles at the vacancies, partially restoring the lost electrons. However, 1.0 wt.% was not sufficient to restore the electrons completely. The Ag3d<sub>5/2</sub> binding energies for Ag, Ag<sub>2</sub>O and AgO are well known to be 368.2, 367.8, and 367.4 eV, respectively [48]. However, XPS spectra allowed us to determine that only one Ag species was present in Ag@Li<sub>0.075</sub>TiO<sub>2</sub>. The binding energies of Ag3d<sub>5/2</sub> and Ag3d<sub>5/7</sub> were observed to be 367.78 and 373.95 eV, which correspond to metallic Ag. From these results, we were able to confirm that Ag was

present in an oxidation state of zero, and that no other oxidation state was present. The metallic state of Ag is known to produce the strongest SPR effect, and therefore we expected to observe photocatalytic activity under visible light [49]. Additionally, the binding energy of Li 1 s was observed to be 54.29 eV for Li<sub>0.075</sub>TiO<sub>2</sub>, which was attributed to Li<sub>2</sub>O, that is, Li<sup>+</sup> [50]. However, in Ag@Li<sub>0.075</sub>TiO<sub>2</sub>, the Li1 s binding energy shifted to a higher energy of 56.18 eV. This was due to the much higher reduction potential of Ag<sup>+</sup>/Ag<sup>0</sup> compared to Li<sup>+</sup> or Ti<sup>4+</sup>; as the Ag ions were loaded, electrons were pulled to from the Li<sub>0.075</sub>TiO<sub>2</sub> particles to produce the reduced form of Ag. Therefore, Ti and Li were present as these more oxidized forms. The elemental analysis results obtained from XPS are shown in atomic % in the table below. The ratio of Ti:O in the cubic TiO<sub>2</sub> was approximately 1:2.2, which was very close to the quantitative value. The Li present in Li<sub>0.075</sub>TiO<sub>2</sub> was approximately

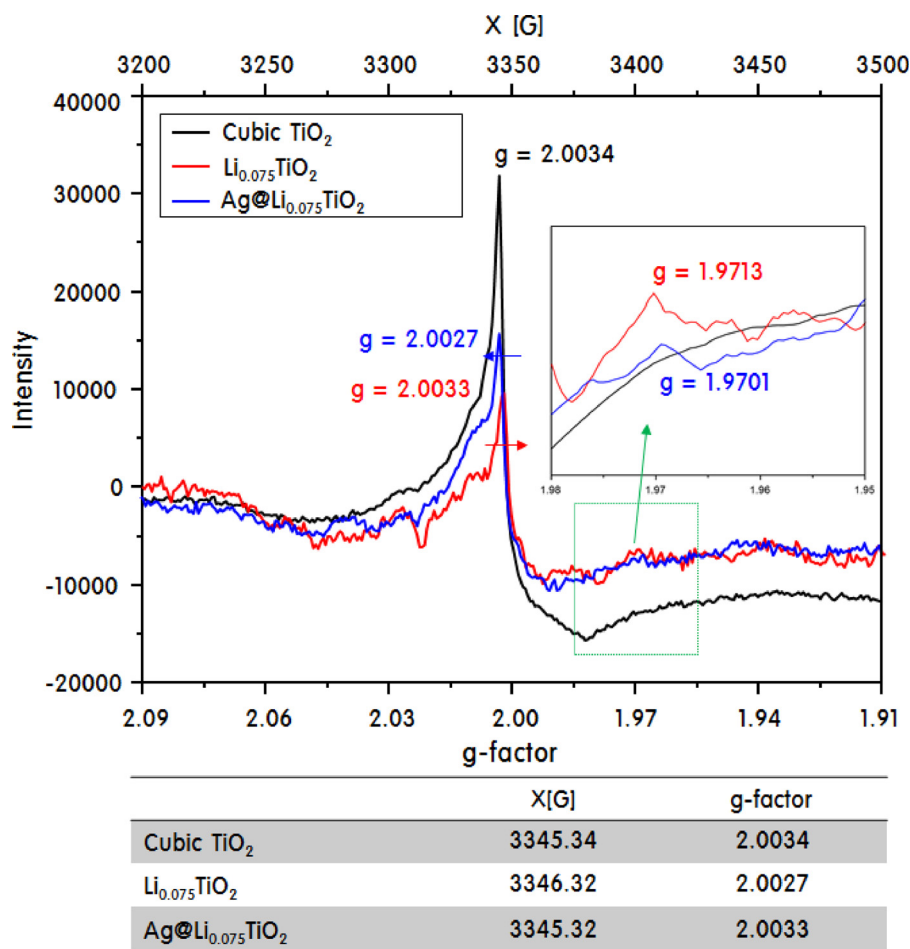


Fig. 9. EPR spectra observed at 77 K for TiO<sub>2</sub>, Li<sub>0.075</sub>TiO<sub>2</sub>, and Ag@Li<sub>0.075</sub>TiO<sub>2</sub> particles.

1.25 atom, which was about 1/25.7 (0.039) the amount of Ti, i.e., 3.9 mol.%, so it was less than half the expected amount. On the other hand, the amount of Ag present in Ag@Li<sub>0.075</sub>TiO<sub>2</sub> is 1.04 atom, which corresponds to 1/30.76 (0.032) of the amount of Ti, so it is about 3.2%, which is three times more than the expected amount. We had to recognize that there is a measurement limit of surface analysis.

In order to obtain accurate information on the presence of oxygen defects (vacancies) in the lattices of the three particles, EPR analysis was attempted and the results are shown in Fig. 9. A unique EPR signal at  $g = 2.00$  was observed in three particles of TiO<sub>2</sub>, Li<sub>0.075</sub>TiO<sub>2</sub>, and Ag@Li<sub>0.075</sub>TiO<sub>2</sub> at room temp. The signal was however about twice more intense in the case of the TiO<sub>2</sub> compared to Li<sub>0.075</sub>TiO<sub>2</sub> and Ag@Li<sub>0.075</sub>TiO<sub>2</sub> particles. In some papers [51], the EPR signal at  $g = 2.00$  was assumed to be closely related to oxygen vacancies concentration. But, generally  $g$  value classically corresponds to the signature of a transition metal element than that an electron trapped in oxygen vacancy expected around  $g = 2.01$ . Thus, the signal for electronic configuration of  $0 < d < 5$  should be reduced or oxidized in the pretreatment conditions such as heating or freezing under inert or oxygenated flow, respectively, and generally the paramagnetic in its reduced form appears at  $g < 2.00$  [52]. As like assumption in all of EPR papers, the possible involvement of two trapped electrons defects is considered in the doublet signals. In order to know the direct involvement of Ti<sup>3+</sup> in the EPR signal, the spectrums are recorded at 77 K in this study because the detecting EPR signal for the chemical mixture is difficult at room temperature. As the result, the EPR signals were observed at  $g = 1.97$  in Li<sub>0.075</sub>TiO<sub>2</sub> and Ag@Li<sub>0.075</sub>TiO<sub>2</sub> particles, whereas no signal was observed in cubic TiO<sub>2</sub> particle. Some papers reported the EPR signal of Ti<sup>3+</sup> at  $g = 1.96$  having anion vacancies in its

coordination sphere, and additionally the existence of Ti<sup>3+</sup> is known to be sensitive to the high photocatalytic performance [53]. In this study, the signal of Li<sub>0.075</sub>TiO<sub>2</sub> at  $g = 1.97$  was strong compared to Ag@Li<sub>0.075</sub>TiO<sub>2</sub>, means its high density for metal atom per volume of solid and an increase of oxygen vacancies in Li<sub>0.075</sub>TiO<sub>2</sub>. Meanwhile, the Li<sub>0.075</sub>TiO<sub>2</sub> could be inferred that the electron released upon oxygen vacancy formation could be trapped as quasi free electron at particular oxygen vacancies in close interaction between  $d$  orbital of Ti and impurities such as Li. Here, a slightly decrease in oxygen vacancies in Ag@Li<sub>0.075</sub>TiO<sub>2</sub> seems to be due to that Ag was more grown on the oxygen vacancy to be stably anchored on the surface of Li<sub>0.075</sub>TiO<sub>2</sub> as already mentioned in HRTEM result of Fig. 7.

#### 3.4. Photocatalytic performance on Ag@Li<sub>0.075</sub>TiO<sub>2</sub> particle

The CO<sub>2</sub> photo-reduction reactions were performed on cubic TiO<sub>2</sub>, Ag@TiO<sub>2</sub>, Li<sub>0.075</sub>TiO<sub>2</sub>, and Ag@Li<sub>0.075</sub>TiO<sub>2</sub> under UV light of 365 nm, and the results are displayed in Fig. 10. The main product obtained in the rate-determining step of the photoreduction of CO<sub>2</sub> is CO, followed by other reduction products including HCHO, CH<sub>3</sub>OH, and CH<sub>4</sub> [54]. Under UV irradiation, the ratio of the formation of CO and CH<sub>4</sub> was 1:1 after 10 h of reaction using the cubic TiO<sub>2</sub> catalyst, while approximately 98% CH<sub>4</sub> (20 μmol/g) was produced after 10 h of reaction using the Ag@TiO<sub>2</sub> catalyst. Using the Li<sub>0.075</sub>TiO<sub>2</sub> catalyst, the product ratio of CO and CH<sub>4</sub> was also 1:1, but the product selectivity with Ag nanoparticle shifted towards CH<sub>4</sub>, and the product ratio of CH<sub>4</sub> to CO was about 3:1. Finally, the CH<sub>4</sub> production of Ag@Li<sub>0.075</sub>TiO<sub>2</sub> was 49 μmol/g after 10 h of reaction, which was 1.5 times greater than that of Li<sub>0.075</sub>TiO<sub>2</sub> (33 μmol/g) under UV light. This result confirmed that the

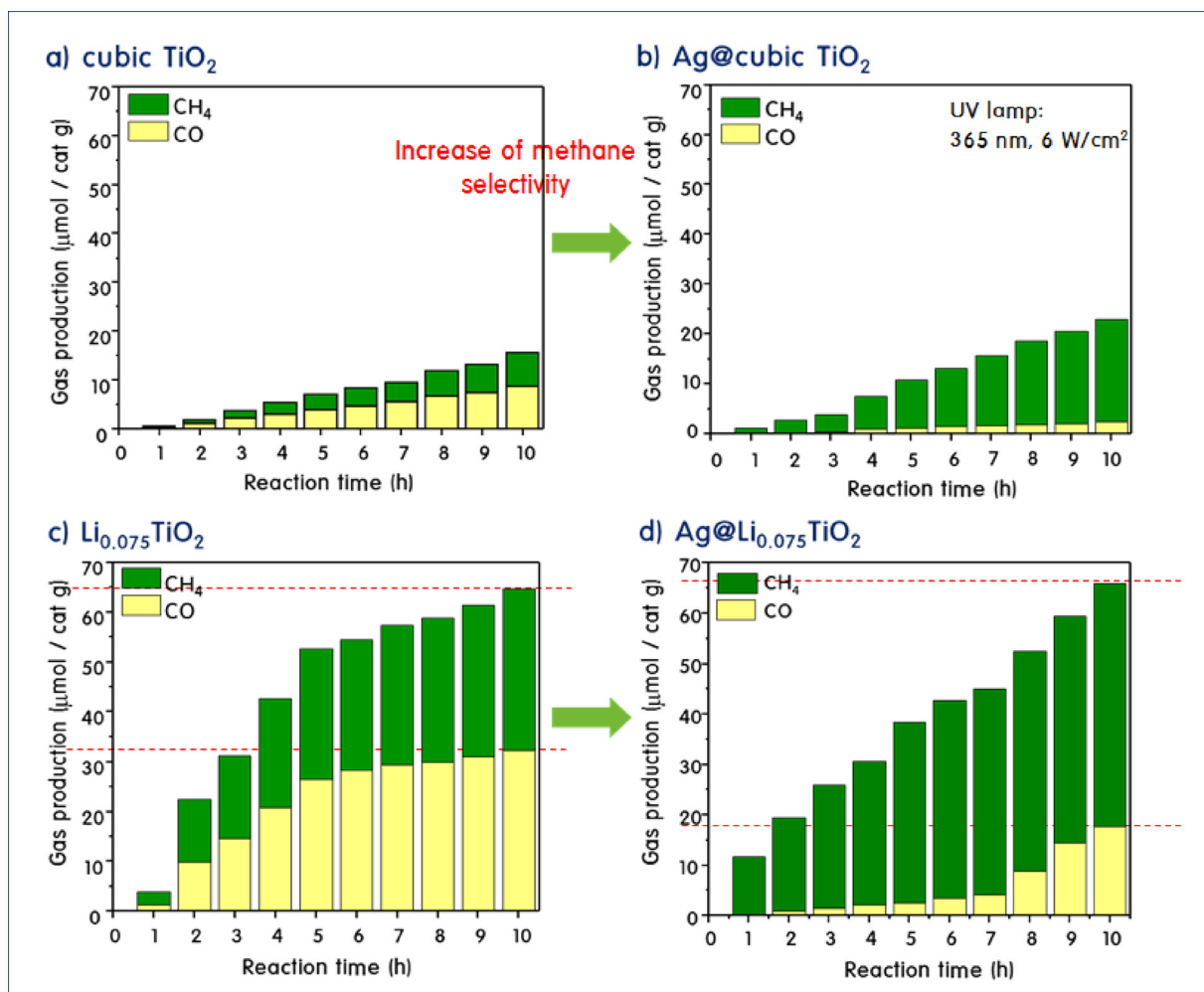


Fig. 10. Catalytic performances for CO<sub>2</sub> photoreduction on cubic TiO<sub>2</sub>, Ag@TiO<sub>2</sub>, Li<sub>0.075</sub>TiO<sub>2</sub>, and Ag@Li<sub>0.075</sub>TiO<sub>2</sub> particles under UV-light irradiation.

CH<sub>4</sub> was selectively obtained by the addition of Ag.

In order to observe the SPR effect of Ag, the photo-reduction reactions were conducted under visible lights of 420 and 620 nm as shown in Fig. 11A. The photocatalytic activity of the Ag@Li<sub>0.075</sub>TiO<sub>2</sub> particle did not decrease under both visible lights, and showed activity similar to that observed under UV light, with a CH<sub>4</sub> yield of 42 and 34 μmol/g at 420 and 620 nm after 10 h, respectively. Generally, since the plasmonic absorption of Ag is located in the visible light range around 450 nm, the visible light-active plasmonic metal can be utilized as a visible-light sensitizer for TiO<sub>2</sub> with a wide band-gap for achieving visible light photocatalytic CO<sub>2</sub> reduction. Eventually, this could be assumed due to the strong SPR effect of the Ag metal particles, as generally TiO<sub>2</sub> has little optical activity in the visible range due to its wide band gap [55]. As mentioned above, it is difficult to discuss the SPR effect of small metal nanoparticles with 10 nm or less. Moreover, since the particle size is small, the exposed growth facets cannot be reliably known, and therefore the activation energy between the exposed growth facets and the adsorbed reactants cannot be obtained, so that the selectivity of the product cannot be theoretically discussed therefrom. In particular, the particle sizes of Ag in the samples prepared in this study were very small about 0.5 nm, and thus the product selectivity according to the exposed growth facets could not discuss. Furthermore, there are a number of papers predicting the relationship between the exposed growth facets and product selectivities on the main TiO<sub>2</sub> catalyst (or TiO<sub>2</sub>-like) [56–58]. However, there are few studies about the relation between the growth facet and product selectivity on metal nanoparticles that exhibited the SPR effect. Only a

few studies have confirmed the selectivity of the product depending on the size or loading of metal nanoparticles [59,60]. As mentioned in introduction, Li and his colleagues announced the results that when loading 0.5 wt.% of Ag into a brookite type TiO<sub>2</sub> nanocube, CO<sub>2</sub> was selectively reduced into CO over the [210] facet of TiO<sub>2</sub>, and when the amount of Ag was increased to 1.0 wt.% loading, the CO<sub>2</sub> was selectively reduced to CH<sub>4</sub> over [001] facet of TiO<sub>2</sub>. However, when Ag was loaded more than 5.0 wt.%, the Ag nanoparticles aggregated or decomposed, the adsorptions of H<sub>2</sub>O and CO<sub>2</sub> were competitive, resulting in both selectivities of CH<sub>4</sub> and CO decreased [11]. Liu et al. also presented that when the concentration of Ag was increased to 0.7 mmol in the Ag/TiO<sub>2</sub> nano-wire films, the PSR effect of Ag promoted CO<sub>2</sub> photo-reduction and increased the selectivity to CH<sub>3</sub>OH [61]. In addition, Tahir et al. found out that the synergistic effect in plasmonic Au/Ag alloy nanoparticles for selective photocatalytic CO<sub>2</sub> reduction with H<sub>2</sub> into CO and hydrocarbons under visible light irradiation. They addressed that the plasmonic Au/Ag nanoparticles co-decorated TiO<sub>2</sub> nano-wires led to the enhanced photoactivity on CO<sub>2</sub> reduction into CO [62]. These studies mean that depending on the crystal morphology, the crystal structure type, and the exposed growth facet of the main catalyst and the kinds of metal nanoparticles loaded (which express the SPR effect) and the sizes, the selectivities of the products produced in catalytic reactions can vary. In conclusion, the growth facet [101] of cubic Li<sub>x</sub>TiO<sub>2</sub> was activated and selectivity to CH<sub>4</sub> increased by 1.0 wt.% Ag loading in this study. To be more specific, the loaded fine Ag nanoparticle was located on the state between the valence band and the conduction band of Li<sub>x</sub>TiO<sub>2</sub> and to generate the mid-gap states. Here the



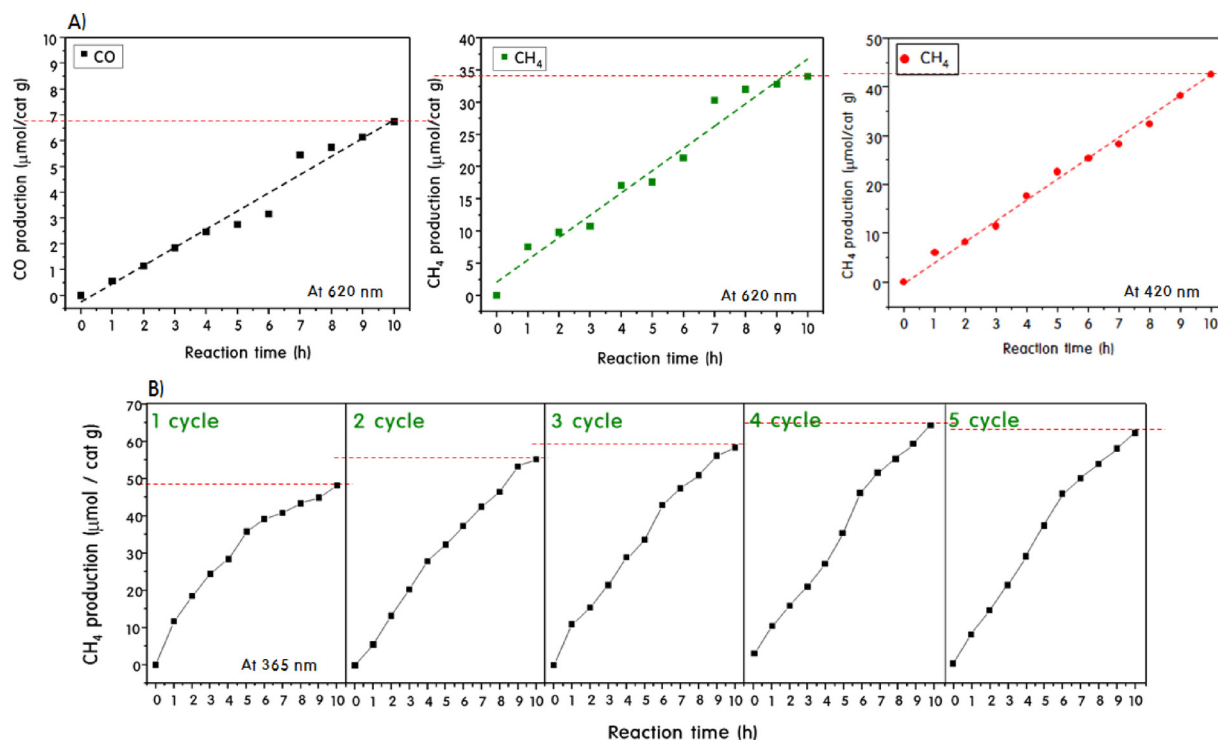
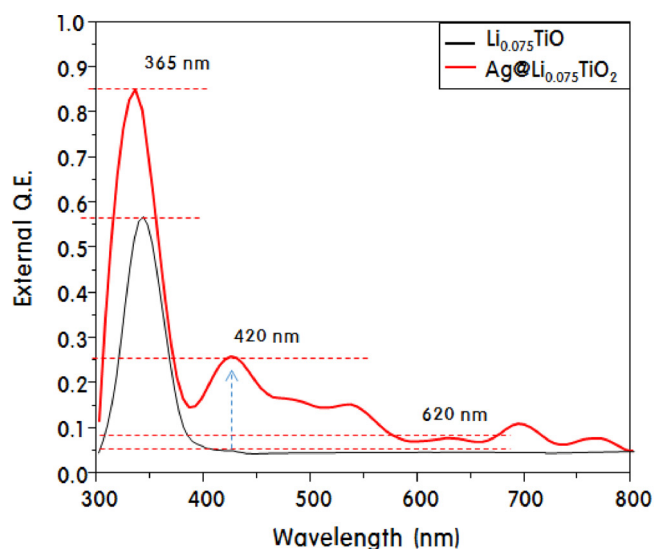


**Fig. 11.** Catalytic performances for CO<sub>2</sub> photoreduction on Ag@Li<sub>0.075</sub>TiO<sub>2</sub> particle under visible light irradiation (A) and recycling test for CO<sub>2</sub> photoreduction on Ag@Li<sub>0.075</sub>TiO<sub>2</sub> particle under UV-light irradiation (B).

mid-gap states led to the charge donation and withdrawing from Ag, thus these features enhanced the photo response of TiO<sub>2</sub> or Li<sub>x</sub>TiO<sub>2</sub>, contributed to increase the lifetime of the photo generated electron – hole pairs (excitons) and the catalytic activity on CO<sub>2</sub> reduction. Meanwhile, the most important aspect of a catalyst is its lifetime; thus, it is essential to perform a recycling test on the catalyst. The recycling experiments on Ag@Li<sub>0.075</sub>TiO<sub>2</sub> were performed for five cycles under UV light irradiation of 365 nm, and the results are presented in Fig. 11B. Specifically, after 10 h of reaction, the light was turned off, the reactor was disassembled to remove the catalyst, and the catalyst was kept in a dark room for 24 h. The gas inside the reactor was purged and released. The reactor was then reassembled, and the catalyst that was stored in a dark room for 24 h was again fixed in the reactor. Water was added to the reactor, and the reactor was purged with nitrogen to remove the air inside the reactor. After injecting carbon dioxide into the reactor, the reactor was packed and the reaction was started by turning on the light source. After 10 h of reaction, the reaction was stopped and the catalyst was again kept in the dark for 24 h. This procedure was repeated five times. Approximately 49 μmol/g of CH<sub>4</sub> was produced in the first cycle and it largely increased to 55 μmol/g in the second cycle. This is probably due to that until the second cycle, the surface of the catalyst is unstable, and the reactants adsorbed on the surface of the catalyst in first cycle reaction are separated and reacted together. Therefore, more reactants are reacted than the actual reaction in the second cycle, so that more products are produced. However, as the reaction cycle increases, since the catalyst surface is completely stabilized and saturated. Therefore, in the continuous system, the catalytic reaction takes place almost constantly, until the catalyst deterioration occurs. Eventually, it was 58 μmol/g in the third cycle, and 65 μmol/g in the fourth cycle. With each subsequent cycle, the yield did not decrease, but instead increased. In the fifth cycle, however, the yield decreased slightly to 62 μmol/g. These results implied that the Ag@Li<sub>0.075</sub>TiO<sub>2</sub> catalyst remained stable even when exposed to light. The reason for this was presumably that Ag was present in a single stable oxidation state as metallic Ag, and was stably fixed at the defect sites of the crystal lattice.

In general, the activity of the catalyst is closely related to the wavelength of the light source. IPCE indicates the number of incident photons inside the cell and their contribution to the efficiency. IPCE is defined as the ratio of electrons in the external circuit produced by an incident photon at a given wavelength. Fig. 12 shows the quantum efficiency obtained from the IPCE spectra according to the irradiation wavelength for Li<sub>0.075</sub>TiO<sub>2</sub> and Ag@Li<sub>0.075</sub>TiO<sub>2</sub> catalysts. Overall, quantum efficiency was improved in samples loaded with Ag at all wavelengths. Li<sub>0.075</sub>TiO<sub>2</sub> showed the maximum quantum efficiency of 0.56 at 365 nm, and it was largely decreased in the wavelength region after 400 nm. However, on the Ag@Li<sub>0.075</sub>TiO<sub>2</sub> catalyst, various quantum efficiencies were observed at wavelengths of 365, 420, 520, 620 and 720 nm. The maximum quantum efficiency was 0.85 in the UV wavelength range of 365 nm and was reduced to 0.25 at 420 nm. Comparing the increase and decrease of quantum efficiency by loading Ag on Li<sub>0.075</sub>TiO<sub>2</sub>, the 0.56 of quantum efficiency of Li<sub>0.075</sub>TiO<sub>2</sub> at 365 nm showed an increase of 29% into 0.85 for Ag@Li<sub>0.075</sub>TiO<sub>2</sub>. At 420 and 620 nm, the quantum efficiencies of 0.05 and 0.04 for Li<sub>0.075</sub>TiO<sub>2</sub> increased by 20% and 4%, respectively, into 0.25 and 0.08 for Ag@Li<sub>0.075</sub>TiO<sub>2</sub>. Lu et al. reported that the addition of Ag and TiO<sub>2</sub> to the Schottky junction at the interface between Ag and TiO<sub>2</sub> also enhanced the absorption of visible light due to SPR effect [63]. Additionally, after loading Ag on Li<sub>0.075</sub>TiO<sub>2</sub>, the CO<sub>2</sub> reduction slightly increased from 65% (Li<sub>0.075</sub>TiO<sub>2</sub>) to 66% (Ag@Li<sub>0.075</sub>TiO<sub>2</sub>) under UV light. Under UV irradiation, the quantum efficiency was also larger on Ag@Li<sub>0.075</sub>TiO<sub>2</sub> than on Li<sub>0.075</sub>TiO<sub>2</sub>, but the CO<sub>2</sub> photoreduction did not increase significantly. Perhaps this is considered to a reason that Ag did not express the SPR effect under UV irradiation. From these results, we were convinced that the SPR effect is independent of the catalytic performance under the UV light irradiation. On the other hand, the CO<sub>2</sub> photoreduction rarely occurred on Li<sub>0.075</sub>TiO<sub>2</sub> under the visible lights of 420 and 620 nm. This is because the band-gap energy of Li<sub>0.075</sub>TiO<sub>2</sub> was larger than the energy of the light source, so that the electrons were not excited. On the other hand, Ag@Li<sub>0.075</sub>TiO<sub>2</sub> activated the CO<sub>2</sub> photoreduction under 420 and 620 nm wavelengths and showed a total product yield of 52.1 and 39.8%, which was attributed to the loading of



Cubic $\text{Li}_{0.075}\text{TiO}_2$			$\text{Ag@Li}_{0.075}\text{TiO}_2$	
	Q.E	Total yield of products ( $\mu\text{mol}/\text{cat} \cdot \text{g}$ )	Q.E	Total yield of products ( $\mu\text{mol}/\text{cat} \cdot \text{g}$ )
365 nm	0.56	65	0.85	66
420 nm	0.05	-	0.25	52.1
620 nm	0.04	-	0.08	39.8

Fig. 12. Quantum efficiency obtained from the IPCE spectra according to the irradiation wavelength for  $\text{Li}_{0.075}\text{TiO}_2$  and  $\text{Ag@Li}_{0.075}\text{TiO}_2$  particles.

plasmonic Ag metal absorbed at 460 nm. The beneficial effects of Ag loading on  $\text{Li}_{0.075}\text{TiO}_2$  was a significantly enhancement of the photocatalytic activity under visible light irradiation, in particular around 420 nm. These results may be explained in terms of the different roles of Ag in affecting the photocatalytic behaviors of  $\text{Ag@Li}_{0.075}\text{TiO}_2$  under UV and visible light irradiation in  $\text{CO}_2$  photoreduction mechanism.

To compare the recombination lifetime and electron transport time in  $\text{Li}_{0.075}\text{TiO}_2$  and  $\text{Ag@Li}_{0.075}\text{TiO}_2$ , IMVS and IMPS measurements were carried out. Typical IMVS responses are presented in Fig. 13A and B. The IMVS circle was shifted to the left in the  $\text{Ag@Li}_{0.075}\text{TiO}_2$  spectra compared to its position in the  $\text{Li}_{0.075}\text{TiO}_2$  spectra. This shift indicated slower recombination between electrons and holes in  $\text{Ag@Li}_{0.075}\text{TiO}_2$  than in  $\text{Li}_{0.075}\text{TiO}_2$ . The recombination time ( $s$ , y-axis) was determined using the expression  $s = 1/2pf_r$ , where  $f_r$  is the characteristic frequency minimum of the imaginary IMVS component [64]. Based on the  $s$  value and current intensity of all the samples, a correlation was drawn, as shown in Fig. 13C. Recombination was faster at higher current in  $\text{Li}_{0.075}\text{TiO}_2$ , and this trend was substantially greater for the  $\text{Ag@Li}_{0.075}\text{TiO}_2$ ; however, the recombination time of  $\text{Ag@Li}_{0.075}\text{TiO}_2$  was still slow compared to  $\text{Li}_{0.075}\text{TiO}_2$ . This may be due to the electron trapping effect due to the SPR effects of Ag in  $\text{Ag@Li}_{0.075}\text{TiO}_2$ . In other words, because Ag can attract the electrons flowing in from an external circuit, no electrons are dropped, and as a result the recombination time is slow. The limitations of the photocurrent density have marked effects on the IMPS response. Electron transport times ( $s$ , y-axis) can be estimated from IMPS plots using the expression  $s = 1/2pf_t$  [65], where  $f_t$  is the characteristic frequency at the minimum value of the imaginary component of IMPS. The IMPS time constant is determined by the transport time needed for the electrons to move from the point at which they are generated to the conductive back contact, and by the electron lifetime. Therefore, it is reasonable to use the IMPS to determine the electron transport time. The transport time constant affects the

measured IMPS signals at high frequencies. The Ag in  $\text{Ag@Li}_{0.075}\text{TiO}_2$  can trap/de-trap the electrons, which could make the electron transport time significantly faster than in  $\text{Li}_{0.075}\text{TiO}_2$ , as shown in Fig. 13D. Additionally, higher light intensities will lead to the filling of traps to a higher energy, resulting in faster electron transport. The observed transport time in  $\text{Li}_{0.075}\text{TiO}_2$  can be explained by a distribution of traps that increases exponentially from the valence band to the conduction band, while the transport time in  $\text{Ag@Li}_{0.075}\text{TiO}_2$  can be explained by a distribution of traps forward the conduction band on  $\text{Li}_{0.075}\text{TiO}_2$  from Ag by the effect of SPR of Ag. These results imply direct electron transfer (DET) and plasmonic resonant energy transfer (PRET), which are characteristics of metals that exhibit SPR [66]. Thus, in this work, the improved photoactivity was attributed to the surface plasmon resonance of Ag, in particular via DET or PRET to the conduction band of  $\text{Li}_x\text{TiO}_2$ .

Finally, we present two catalytic mechanisms under UV and visible light irradiations in Scheme 1. As shown in Scheme 1A,  $\text{Li}_x\text{TiO}_2$  absorbs UV light, and electrons are transferred from the valence band to the conduction band. These electrons are trapped by Ag, which has a strong reduction potential, leading to effective charge separation, and thus the photocatalytic performance can be maintained for a long time. In the valence band of  $\text{Li}_x\text{TiO}_2$ , water is decomposed to produce  $\text{H}^+$ , and on the conduction band or Ag surface,  $\text{CO}_2$  is reduced to  $\text{CO}$  or  $\text{CO}_2^-$ , and  $\text{H}^+$  takes electrons and goes to  $\cdot\text{H}$  radical. Finally, four  $\cdot\text{H}$  radicals react with  $\text{CO}$  or  $\cdot\text{C}$  radical to produce  $\text{CH}_4$ . These products are produced by a mechanism in which one electron participates ( $\text{CO}_2^-$  generation) and a mechanism in which two electrons participate ( $\text{CO}$  generation), with the latter being favored [67]. As described in the gas adsorption results, since the adsorption of  $\text{CO}_2$  is most likely to take place at the oxygen vacancy sites (Scheme 1A-a), the rate of generation of  $\text{CO}$  in the rate-determining step is expected to be fast. Also, as noted in the introduction, Ag-TiO<sub>2</sub> is known to act as a catalyst for hydrogen production by decomposing water [29], thus increasing the selectivity for  $\text{CH}_4$  by promoting  $\text{H}_2$  production on Ag. The stoichiometric conversion of  $\text{CO}_2$  to  $\text{CH}_4$  occurs via the following reaction:  $\text{CO}_2 + 4\text{H}_2\text{O} \rightarrow \text{CH}_4 + 2\text{H}_2\text{O} + 2\text{O}_2$ . On the other hand, in the visible region (Scheme 1B), Ag first absorbs light, and then transmits electrons to the conduction band of  $\text{Li}_x\text{TiO}_2$  via its SPR effect.  $\text{CO}_2$  is either reduced by receiving the electrons on the conduction band of  $\text{Li}_x\text{TiO}_2$ . On the other hand,  $\text{H}_2\text{O}$  is transformed from the hole of the valence band of Ag to  $\text{H}^+$ , and then receives electrons from the Ag surface to form  $\cdot\text{H}$  radical, and reacts with the  $\text{CO}$  or  $\cdot\text{C}$  radical on the electron rich conduction band of  $\text{Li}_x\text{TiO}_2$  to form  $\text{CH}_4$ . As already mentioned in the photoactivity results, the SPR effect of Ag was very strong, despite the small Ag content of 1.0 wt.%. This was thought to be due, in particular, to the fact that Ag was stably fixed at the lattice defects and existed in a single oxidation state,  $\text{Ag}^0$ . As a result, it was expected to have strong electron trapping/de-trapping properties with a so-called coupled-SPR effect, which could exhibit synergy with each other even with a small amount of Ag.

#### 4. Conclusions

This study aimed to improve the performance of the photoreduction of  $\text{CO}_2$  to  $\text{CH}_4$ . To this end, cubic-shaped  $\text{Ag@Li}_x\text{TiO}_2$  particles loaded with 1.0 wt.% of silver were prepared. In the  $\text{Ag@Li}_x\text{TiO}_2$  catalyst, the [101] facet of the cubic  $\text{TiO}_2$  was activated, the adsorption of  $\text{CO}_2$  was increased, and the conversion from  $\text{CO}_2$  to  $\text{CO}$  (the rate-determining step in the  $\text{CO}_2$  reduction reaction) was accelerated, and eventually,  $\text{CH}_4$  was selectively generated. In particular, the  $\text{Ag@Li}_{0.075}\text{TiO}_2$  catalyst showed good performance under both UV and visible light because the superfine Ag particles with a size of 0.3–0.5 nm were formed stably at the oxygen defect sites on the  $\text{Li}_{0.075}\text{TiO}_2$  lattice surface and exhibited a strong SPR. In addition, IMVS and IMPS analysis clarified that in  $\text{Ag@Li}_{0.075}\text{TiO}_2$ , good charge separation was achieved and the electron transport rate was fast. Furthermore,  $\text{Ag@Li}_{0.075}\text{TiO}_2$  showed

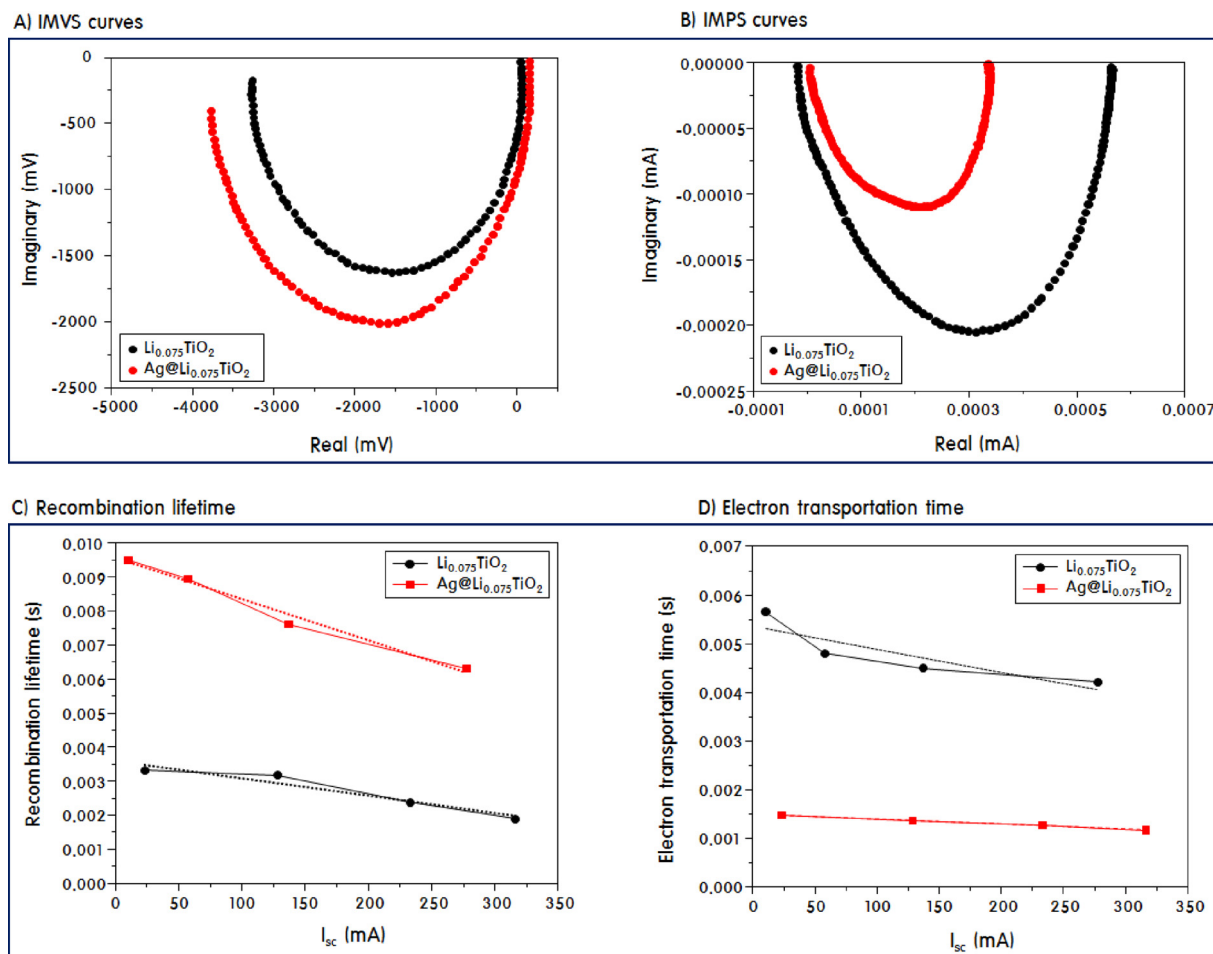
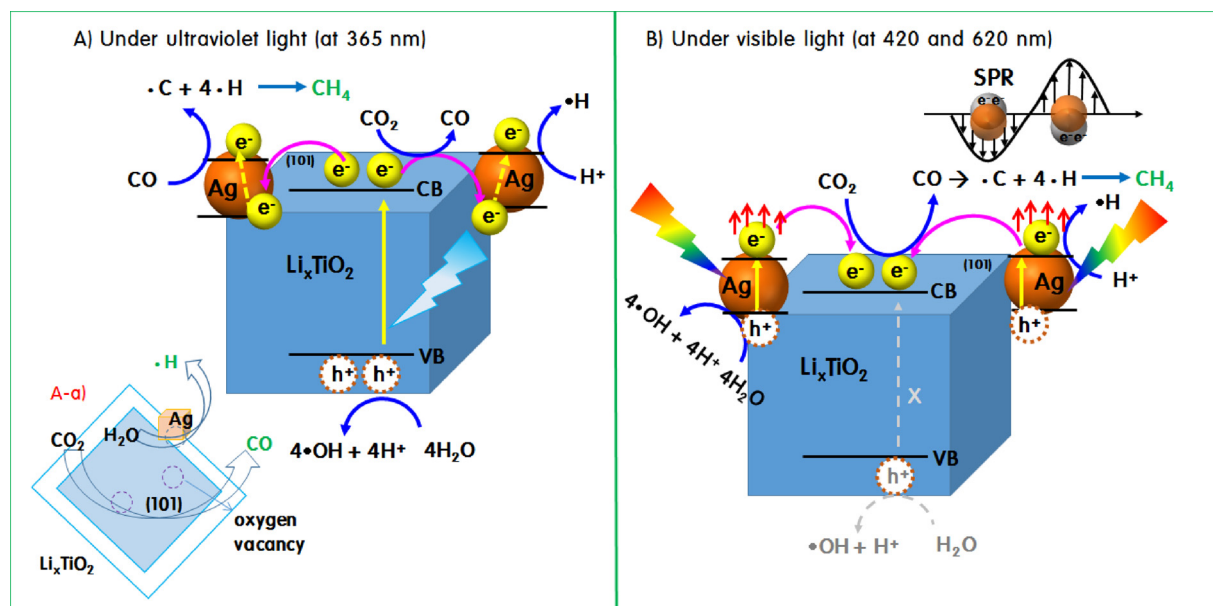


Fig. 13. IMVS (A) and IMPS (B) curves for  $\text{Li}_{0.075}\text{TiO}_2$  and  $\text{Ag@Li}_{0.075}\text{TiO}_2$  particles, and recombination lifetime (C) and electron transport time D) determined from IMVS and IMPS curves, respectively.



Scheme 1. Expected mechanisms for the photoreduction of  $\text{CO}_2$  to  $\text{CH}_4$  on  $\text{Ag@Li}_x\text{TiO}_2$  particle under UV- and visible light irradiations.



no catalytic deterioration in a five-cycle recycling test, with the production of  $\text{CH}_4$  instead increasing to  $65 \mu\text{mol/g}$  in the fourth cycle. Therefore, the  $\text{Ag@Li}_{0.075}\text{TiO}_2$  particles were concluded to be optically stable. Based on these results, we believe that suitable exploitation of the crystal morphology, the oxygen vacancy in lattice, and the SPR properties can contribute greatly to controlling the products of the photoreaction.

## Acknowledgements

This work was conducted under framework of the research and development program of the Korea Institute of Energy Research (B8-2437), and was also supported by the National Research Foundation of Korea (NRF) grant funded by the Korea government (MSIT) (No. 2018R1A2B6004746).

## References

- J. Su, L. Vayssieres, A place in the sun for artificial photosynthesis? *ACS Energy Lett.* 1 (2016) 121–135.
- N. Son, J.Y. Do, M. Kang, Characterization of core@ shell-structured  $\text{ZnO@Sb}_2\text{S}_3$  particles for effective hydrogen production from water photo splitting, *Ceram. Int.* 43 (2017) 11250–11259.
- J. Chae, J. Lee, J.H. Jeong, M. Kang, Hydrogen production from photo splitting of water using the Ga-incorporated  $\text{TiO}_2$ s prepared by a solvothermal method and their characteristics, *Bull. Korean Chem. Soc.* 30 (2009) 302–308.
- R. Sathesh, K. Vignesh, M. Rajarajan, A. Suganthi, S. Sreekantan, M. Kang, B.S. Kwak, Removal of Congo Red from water using quercetin modified  $\alpha\text{-Fe}_2\text{O}_3$  nanoparticles as effective nanoadsorbent, *Mat. Chem. Phys.* 180 (2016) 53–65.
- O.F. Lopes, K.T.G. Carvalho, A.E. Nogueira, W. Avansi Jr, C. Ribeiro, Controlled synthesis of  $\text{BiVO}_4$  photocatalysts: evidence of the role of heterojunctions in their catalytic performance driven by visible-light, *Appl. Catal. B* 188 (2016) 87–97.
- B.S. Kwak, K.M. Kim, S.M. Park, M. Kang, Synthesis of basalt fiber@ $\text{Zn}_{1-x}\text{Mg}_x\text{O}$  core/shell nanostructures for selective photoreduction of  $\text{CO}_2$  to CO, *Appl. Surf. Sci.* 407 (2017) 109–116.
- C. Wang, X. Zhang, B. Yuan, Y. Wang, P. Sun, D. Wang, Y. Wei, Y. Liu, Multi-heterojunction photocatalysts based on  $\text{WO}_3$  nanorods: structural design and optimization for enhanced photocatalytic activity under visible light, *Chem. Eng. J.* 237 (2014) 29–37.
- H. Zhao, F. Pan, Y. Li, A review on the effects of  $\text{TiO}_2$  surface point defects on  $\text{CO}_2$  photoreduction with  $\text{H}_2\text{O}$ , *J. Materiomics* 3 (2017) 17–32.
- X. Zheng, Q. Kuang, K. Yan, Y. Qiu, J. Qiu, S. Yang, Mesoporous  $\text{TiO}_2$  single crystals: facile shape-, size-, and phase-controlled growth and efficient photocatalytic performance, *ACS Appl. Mater. Interf.* 5 (2013) 11249–11257.
- W. Gan, X. Fu, J. Zhang,  $\text{Ag@AgCl}$  decorated graphene-like  $\text{TiO}_2$  nanosheets with nearly 100% exposed (001) facets for efficient solar light photocatalysis, *Mat. Sci. Eng. B* 229 (2018) 44–52.
- K. Li, T. Peng, Z. Ying, S. Song, J. Zhang, Ag-loading on brookite  $\text{TiO}_2$  quasi nanocubes with exposed {210} and {001} facets: activity and selectivity of  $\text{CO}_2$  photoreduction to  $\text{CO/CH}_4$ , *Appl. Catal. B* 180 (2016) 130–138.
- M. Masis, L. Ding, F. Dauzou, Q. Jeangros, A. Wyser, S. Nicolay, C. Ballif, Hydrogen plasma treatment for improved conductivity in amorphous aluminum doped zinc tin oxide thin films, *Appl. Mater.* 2 (096113) (2014) 1–7.
- V. Gupta, N. Madaan, D.S. Jensen, S.C. Kunzler, M.R. Linford, Hydrogen plasma treatment of silicon dioxide for improved silane deposition, *Langmuir* 29 (2013) 3604–3609.
- G.T. Lewis, G.R. Nowling, R.F. Hicks, Y. Cohen, Inorganic surface nanostructuring by atmospheric pressure plasma-induced graft polymerization, *Langmuir* 23 (2007) 10756–10764.
- C.C. Wu, C.I. Wu, J.C. Sturm, A. Kahn, Surface modification of indium tin oxide by plasma treatment: an effective method to improve the efficiency, brightness, and reliability of organic light emitting devices, *Appl. Phys. Lett.* 70 (1997) 1348–1350.
- D. Guitoume, S. Achour, N. Sobti, M. Boudissa, N. Souami, Y. Messaoudi, Structural, optical and photoelectrochemical properties of  $\text{TiO}_2$  films decorated with plasmonic silver nanoparticles, *Optik* 154 (2018) 182–191.
- K. Nakamura, T. Oshikiri, K. Ueno, Y. Wang, Y. Kamata, Y. Kotake, H. Misawa, Properties of plasmon-induced photoelectric conversion on a  $\text{TiO}_2/\text{NiO}$  p–n junction with Au nanoparticles, *J. Phys. Chem. Lett.* 7 (2016) 1004–1009.
- R.K. Chava, S.Y. Oh, Y.T. Yu, Enhanced  $\text{H}_2$  gas sensing properties of  $\text{Au@In}_2\text{O}_3$  core-shell hybrid metal-semiconductor heteronanostructures, *CrystEngComm* 18 (2016) 3655–3666.
- Q. Zhang, D.T. Gangadharan, Y. Liu, Z. Xu, M. Chaker, D. Ma, Recent advancements in plasmon-enhanced visible light-driven water splitting, *J. Materiomics* 3 (2017) 33–50.
- N.C. Jeong, C. Prasittichai, J.T. Hupp, Photocurrent enhancement by surface plasmon resonance of silver nanoparticles in highly porous dye-sensitized solar cells, *Langmuir* 27 (2011) 14609–14614.
- L. Peedikakkandy, P. Bhargava, A study of photocurrent enhancement by Au, Ag and Cu nanoparticles in dye sensitized solar cells, *Adv. Sci. Lett.* 22 (2016) 958–963.
- A.G. Koutsoubas, N. Spiliopoulos, D. Anastassopoulos, A.A. Vradis, G.D. Pifitis, Nanoporous alumina enhanced surface plasmon resonance sensors, *J. Appl. Phys.* 103 (2008) 094521.
- L. Wang, Y. Sun, J. Wang, J. Wang, A. Yu, H. Zhang, D. Song, Preparation of surface plasmon resonance biosensor based on magnetic core/shell  $\text{Fe}_3\text{O}_4/\text{SiO}_2$  and  $\text{Fe}_3\text{O}_4/\text{Ag}/\text{SiO}_2$  nanoparticles, *Colloids Surf. B* 84 (2011) 484–490.
- N.J.M. Sanghamitra, S. Mazumdar, Effect of polar solvents on the optical properties of water- dispersible thiol-capped cobalt nanoparticles, *Langmuir* 24 (2008) 3439–3445.
- K.K. Mandari, B.S. Kwak, A.K.R. Police, M. Kang, In-situ photo-reduction of silver particles and their SPR effect in enhancing the photocatalytic water splitting of  $\text{Ag}_2\text{O}/\text{TiO}_2$  photocatalysts under solar light irradiation: a case study, *Mater. Res. Bull.* 95 (2017) 515–524.
- T. Ghodselahi, M.A. Vesaghi, A. Shafiekhani, Study of surface plasmon resonance of  $\text{Cu@Cu}_2\text{O}$  core-shell nanoparticles by Mie theory, *J. Phys. D: Appl. Phys.* 42 (2009) 1–6.
- J. Singh, K. Sahu, A. Pandey, M. Kumar, T. Ghosh, B. Satpati, T. Som, S. Varma, D.K. Avasthi, S. Mohapatra, Atom beam sputtered  $\text{Ag-TiO}_2$  plasmonic nano-composite thin films for photocatalytic applications, *Appl. Surf. Sci.* 411 (2017) 347–354.
- J. Low, S. Qiu, D. Xu, C. Jiang, B. Cheng, Direct evidence and enhancement of surface plasmon resonance effect on Ag-loaded  $\text{TiO}_2$  nanotube arrays for photocatalytic  $\text{CO}_2$  reduction, *Appl. Surf. Sci.* 434 (2018) 423–432.
- J.-W. Park, M. Kang, Synthesis and characterization of  $\text{Ag}_x\text{O}$ , and hydrogen production from methanol photodecomposition over the mixture of  $\text{Ag}_x\text{O}$  and  $\text{TiO}_2$ , *Int. J. Hydrogen Energy* 32 (2007) 4840–4846.
- H. Lee, B.S. Kwak, N. Park, J. Baek, H. Ryu, M. Kang, Assembly of a check-patterned  $\text{CuS}_x\text{-TiO}_2$  film with an electron-rich pool and its application for the photoreduction of carbon dioxide to methane, *Appl. Surf. Sci.* 393 (2017) 385–396.
- M. Wagemaker, W.J.H. Borghols, F.M. Mulder, Large impact of particle size on insertion reactions. A case for anatase  $\text{LiTiO}_2$ , *J. Am. Chem. Soc.* 129 (2007) 4324–4327.
- J. Pan, G. Liu, G.Q. Lu, H.M. Cheng, On the true photoreactivity order of {001}, {010}, and {101} facets of anatase  $\text{TiO}_2$  crystals, *Angew. Chem. Int. Ed.* 50 (2011) 2133–2137.
- J. Yan, G. Wu, N. Guan, L. Li, Z. Li, X. Cao, Understanding the effect of surface/bulk defects on the photocatalytic activity of  $\text{TiO}_2$ : anatase versus rutile, *Phys. Chem. Chem. Phys.* 15 (2013) 10978–10988.
- J.I. Langford, A.J.C. Wilson, Scherrer after sixty years: a survey and some new results in the determination of crystallite size, *J. Appl. Cryst.* 11 (1978) 102–113.
- J. Lee, J. Chae, K. Nahm, M. Kang, Synthesis of nanometer-sized hexagonal disk-shaped ZnO in formic acid using a hydrothermal method and its optical properties, *J. Ind. Eng. Chem.* 15 (2009) 645–648.
- S.S. Boxi, S. Paria, Visible light induced enhanced photocatalytic degradation of organic pollutants in aqueous media using Ag doped hollow  $\text{TiO}_2$  nanospheres, *RSC Adv.* 5 (2015) 37657–37668.
- G. Lee, M.-K. Yeo, M.-H. Um, M. Kang, High-efficiently photoelectrochemical hydrogen production over Zn-incorporated nanotubes, *Int. J. Photoenergy* (2012) 843042.
- X. Zheng, L. Zhang, Photonic nanostructures for solar energy conversion, *Energy Environ. Sci.* 9 (2016) 2511–2532.
- D.K. Sarkar, N. Saleema, One-step fabrication process of superhydrophobic green coatings, *Surf. Coat. Technol.* 204 (2010) 2483–2486.
- X. Xiao, L. Ge, C. Han, Y. Li, Z. Zhao, Y. Xin, S. Fang, L. Wu, P. Qiu, A facile way to synthesize  $\text{Ag@AgBr}$  cubic cages with efficient visible-light-induced photocatalytic activity, *Appl. Catal. B* 163 (2015) 564–572.
- N. Zhang, M. Li, C.F. Tan, C.K.N. Peh, T.C. Sum, G.W. Ho, Plasmonic enhanced photoelectrochemical and photocatalytic performances of 1D coaxial  $\text{Ag@Ag}_2\text{S}$  hybrids, *J. Mater. Chem. A* 5 (2017) 21570–21578.
- P. Strobbia, E. Languirand, B.M. Cullum, Recent advances in plasmonic nanostructures for sensing: a review, *Opt. Eng.* 54 (10) (2015) 100902.
- V. Amendola, O.M. Bakr, F. Stellacci, A study of the surface plasmon resonance of silver nanoparticles by the discrete dipole approximation method: effect of shape, size, structure, and assembly, *Plasmonic* 5 (2010) 85–97.
- S. Peng, J.M. McMahon, G.C. Schatz, S.K. Gray, Y. Sun, Reversing the size-dependence of surface plasmon resonances, *PNAS* 107 (33) (2010) 14530–14534.
- W. Deng, Q. Dai, Y. Lao, B. Shi, X. Wang, Low temperature catalytic combustion of 1,2-dichlorobenzene over  $\text{CeO}_2\text{-TiO}_2$  mixed oxide catalysts, *Appl. Catal. B* 181 (2016) 848–861.
- G. Chen, W. Zhou, D. Guan, J. Sunarso, Y. Zhu, X. Hu, W. Zhang, Z. Shao, Two orders of magnitude enhancement in oxygen evolution reactivity on amorphous  $\text{Ba}_{0.5}\text{Sr}_{0.5}\text{Co}_{0.8}\text{Fe}_{0.2}\text{O}_{3-\delta}$  nanofilms with tunable oxidation state, *Sci Adv.* 3 (2017) 1–8.
- Y. Qing, C. Yang, N. Yu, Y. Shang, Y. Sun, L. Wang, C. Liu, Superhydrophobic  $\text{TiO}_2$ /polyvinylidene fluoride composite surface with reversible wettability switching and corrosion resistance, *Chem. Eng. J.* 290 (2016) 37–44.
- N. Wei, H. Cui, Q. Song, L. Zhang, X. Song, K. Wang, Y. Zhang, J. Li, J. Wen, J. Tian,  $\text{Ag}_2\text{O}$  nanoparticle/ $\text{TiO}_2$  nanobelt heterostructures with remarkable photo-response and photocatalytic properties under UV, visible and near-infrared irradiation, *Appl. Catal. B* 198 (2016) 83–90.
- X. Fan, J. Wan, E. Liu, L. Sun, Y. Hu, H. Li, X. Hu, J. Fan, High-efficiency photoelectrocatalytic hydrogen generation enabled by Ag deposited and Ce doped  $\text{TiO}_2$  nanotube arrays, *Ceram. Int.* 41 (2015) 5107–5116.
- S.A. Sharma, Template-free synthesis of hollow  $\text{Li}_2\text{O-Fe}_2\text{O}_3\text{-Ag}$  heterostructures for ultra-high performance Li-ion batteries, *J. Mat. Chem. A* 5 (2017) 14220–14229.
- K. Teramura, T. Tanaka, H. Ishikawa, Y. Kohno, T. Funabiki, Photocatalytic

- reduction of CO<sub>2</sub> to CO in the presence of H<sub>2</sub> or CH<sub>4</sub> as a reductant over MgO, *J. Phys. Chem. B* 108 (2004) 346–354.
- [52] C. Drouilly, J.-M. Krafft, F. Averseng, S. Casale, D. Bazer-Bachi, C. Chizallet, V. Lecocq, H. Vezin, H. Lauron-Pernot, G. Costentin, ZnO oxygen vacancies formation and filling followed by in situ photoluminescence and in situ EPR, *J. Phys. Chem. C* 116 (2012) 21297–21307.
- [53] J. Swaminathan, S. Ravichandran, Insights into the electrocatalytic behavior of defect-centered reduced titania(TiO<sub>1.23</sub>), *J. Phys. Chem. C* 122 (2018) 1670–1680.
- [54] X. Zhang, Z. Zhang, J. Li, X. Zhao, D. Wu, Z. Zhou, Ti<sub>2</sub>CO<sub>2</sub>MXene: a highly active and selective photocatalyst for CO<sub>2</sub> reduction, *J. Mater. Chem. A* 5 (2017) 12899–12903.
- [55] G. Wang, X. Xiao, W. Li, Z. Lin, Z. Zhao, C. Chen, C. Wang, Y. Li, X. Huang, L. Miao, C. Jiang, Y. Huang, X. Duan, Significantly enhanced visible light. photoelectrochemical activity in TiO<sub>2</sub> nanowire arrays by nitrogen implantation, *Nano Lett.* 15 (2015) 4692–4698.
- [56] L. Liu, Y. Jiang, H. Zhao, J. Chen, J. Cheng, K. Yang, Y. Li, Engineering co-exposed {001} and {101} facets in oxygen-deficient TiO<sub>2</sub> nanocrystals for enhanced CO<sub>2</sub> photoreduction under visible light, *ACS Catal.* 6 (2) (2016) 1097–1108.
- [57] Z. Jiang, Q. Ouyang, B. Peng, Y. Zhang, L. Zan, Ag size-dependent visible-light-responsive photoactivity of Ag–TiO<sub>2</sub> nanostructure based on surface plasmon resonance, *J. Mater. Chem. A* 2 (2014) 19861–19866.
- [58] J. Low, B. Cheng, J. Yu, Surface modification and enhanced photocatalytic CO<sub>2</sub> reduction performance of TiO<sub>2</sub>: a review, *Appl. Surf. Sci.* 392 (2017) 658–686.
- [59] M. Wang, Q. Han, Y. Zhou, P. Li, W. Tu, L. Tang, Z. Zou, TiO<sub>2</sub> nanosheet-anchoring Au nanoplates: highenergy facet and wide spectra surface plasmonpromoting photocatalytic efficiency and selectivity for CO<sub>2</sub> reduction, *RSC Adv.* 6 (2016) 81510–81516.
- [60] N. Seriani, C. Pinilla, Y. Crespo, Presence of gap states at Cu/TiO<sub>2</sub> anatase surfaces: consequences for the photocatalytic activity, *J. Phys. Chem. C* 119 (12) (2015) 6696–6702.
- [61] E. Liu, Y. Hu, H. Li, C. Tang, X. Hu, J. Fan, Y. Chen, J. Bian, Photoconversion of CO<sub>2</sub> to methanol over plasmonic Ag/TiO<sub>2</sub> nano-wire films enhanced by overlapped visible-light-harvesting nanostructures, *Ceram. Int.* 41 (2015) 1049–1057.
- [62] M. Tahir, B. Tahir, N.A. Saidina Amin, Synergistic effect in plasmonic Au/Ag alloy NPs co-coated TiO<sub>2</sub> NWs toward visible-light enhanced CO<sub>2</sub> photoreduction to fuels, *Appl. Catal. B* 204 (5) (2017) 548–560.
- [63] N. Lu, Y. Wang, S. Ning, W. Zhao, M. Qian, Y. Ma, J. Wang, L. Fan, J. Guan, X. Yuan, Design of plasmonic Ag-TiO<sub>2</sub>/H<sub>3</sub>PW<sub>12</sub>O<sub>40</sub> composite film with enhanced sunlight photocatalytic activity towards o-chlorophenol degradation, *Sci. Rep.* 7 (2017) 17298.
- [64] Y.-F. Wang, X.-F. Li, D.-J. Li, Y.-W. Sun, X.-X. Zhang, Controllable synthesis of hierarchical SnO<sub>2</sub> microspheres for dye sensitized solar cells, *J. Power Source* 280 (2015) 476–482.
- [65] S.R. Gajjala, C. Yapa, P. Balaya, Multi-functional photoanode films using EP mesoporous TiO<sub>2</sub> aggregate structure for efficient dye sensitized solar cells, *J. Mater. Chem.* 22 (2012) 10873–10882.
- [66] M. Wang, B.B. Rajeeva, L. Scarabelli, E.P. Perillo, A.K. Dunn, L.M. Liz-Marzan, Y. Zheng, Molecular-fluorescence enhancement via blue-shifted plasmon-induced resonance energy transfer, *J. Phys. Chem. C* 120 (2016) 14820–14827.
- [67] B.S. Kwak, J.Y. Do, N. Park, M. Kang, Surface modification of layered perovskite Sr<sub>2</sub>TiO<sub>4</sub> for improved CO<sub>2</sub> photoreduction with H<sub>2</sub>O to CH<sub>4</sub>, *Sci. Rep.* 7 (2017) 1–15.